Comparative study of $Ag@SnO_2/g-C_3N_4$ and $Ag@SnO_2$ nanostructure based efficient acetone resistive gas sensor

A project work submitted in

partial fulfillment of requirements for the degree of

Master of Science

In

Chemistry

By

YOSHITA KATIYAR

(2K22/MSCCHE/58)

&

ANSHIKA GOYAL

(2K22/MSCCHE/56)

Under the supervision of

Dr. Manish Jain and Dr. Deshraj Meena

Department of Applied Chemistry

DELHI TECHNOLOGICAL UNIVERSITY

(Formerly Delhi College Of Engineering)

Shahbad Daulatpur, Main Bawana Road, Delhi-110042, India

MAY, 2024

DELHI TECHNOLOGICAL UNIVERSITY

CANDIDATE DECLARATION

I/We Yoshita Katiyar (2K22/MSCCHE/58) and Anshika Goyal (2K22/MSCCHE/56) hereby certify that the work which is being presented in the thesis entitled "**Comparative study of Ag@SnO_2/g-C_3N_4 and Ag@SnO_2 nanostructure based efficient acetone resistive gas sensor"** in partial fulfillment of the requirements for the award of the Degree of Master in Science, submitted in the Department of Applied Chemistry, Delhi Technological University is an authentic record of my own work carried out during the period from August 2023 to March 2024 under the supervision of Dr. Manish Jain and Dr. Deshraj Meena.

The matter presented in the thesis has not been submitted by us for the award of any other degree of this or any other institute.

Yoshita Katiyar	Anshika Goyal
(2K22/MSCCHE/58)	(2K22/MSCCHE/56)

DELHI TECHNOLOGICAL UNIVERSITY

CERTIFICATE

Certified that Yoshita Katiyar (2K22/MSCCHE/58) and Anshika Goyal (2K22/MSCCHE/56) has carried out their research work presented in this thesis entitled "**Comparative study of Ag@SnO_2/g-C_3N_4 and Ag@SnO_2 nanostructure based efficient acetone resistive gas sensor"** for the award of Master of Science from the Department of Applied Chemistry, Delhi Technological University, Delhi, under my supervision. The thesis embodies results of original work, and studies are carried out by the students herself and the contents of the thesis do not form the basis for the award of any other degree to the candidate or to anybody else from this or any other University/Institution.

PLACE – DELHI

DATE –

Dr. Manish Jain and Dr. Deshraj Meena

(SUPERVISOR)

ACKNOWLEDGEMENT

The success and outcome of this project required a lot of guidance and assistance from many people and we are extremely fortunate to have got this all along the completion of this project work.

We wish to express our gratitude towards my project supervisor, Dr. Manish Jain, Department of Applied Chemistry and Dr. Deshraj Mena, Department of Applied Physics, Delhi Technological University, Who provided us with a golden opportunity to work under their able guidance. Their advices help us to complete the project on time.

We wish to thank Prof. Anil Kumar, Head of the department of the Applied Chemistry, Delhi Technological University for his constant motivation.

We are very much thankful to Ph.D Scholar Gagan Sharma and Shivani Sangwan for their constant support and fortune enough to get encouragement and guidance from all the teaching staff of the Department of Applied Physics, which helped me in completing our project work.

Finally, yet importantly, we would like to express our heartfelt thanks to our beloved family and friends, who have endured our long working hours and whose motivation kept us going.

Yoshita Katiyar and Anshika Goyal

ABSTRACT

Design of new nanocomposites and heterostructures of SnO_2 can improve its gas sensing properties towards various volatile organic compounds (VOCs). In this study, we have successfully synthesized Ag@SnO_2 and Ag decorated on SnO_2/g-C_3N_4 (Ag@SnO_2/g-C_3N_4) using a facile hydrothermal method. The synthesized nanostructures were subjected to various characterization techniques such as XRD, SEM, EDX, BET, UV-Visible to investigate their structural, morphological, and chemical properties. The XRD results confirms the crystalline nature and rutile phase of the synthesized nanostructures, while SEM micrographs revealed morphological variation along with temperature and high dispersion of g-C_3N_4 nanosheets on the surface of Ag@SnO_2 nanostructure. The gas sensing performance of the samples was evaluated for acetone, with Ag@SnO_2/g-C_3N_4 based resistive gas sensor which exhibited admirable sensitivity towards acetone. The enhanced sensing results of Ag@SnO_2-g-C_3N_4 towards VOCs are attributed to its high surface area and strong interaction between Ag@SnO_2 and g-C_3N_4.

Keywords:

Gas-sensing, nanocomposites, Volatile Organic Compounds, Urea, resistive gas sensor

Contents

LIST OF TABLES

LIST OF FIGURES

LIST OF ABBREVIATIONS AND SYMBOLS

ZnA- $Ag@SnO_2$

ZnC- $Ag@SnO_2/g\text{-}C_3N_4$

XRD- X-ray diffraction

SEM- Scanning electron microscope

EDX- Energy Dispersive X-ray

FTIR- Fourier Transform Infrared Spectroscopy

UV- visible- Ultra violet visible

BET- Brunauer-Emmett-Teller

MOS- Metal Oxide Semiconductor

PVD- Physical vapour deposition

CVD- Chemical vapour deposition

VOCs- Volatile organic compound

STP- Standard temperature & pressure

DI- Distilled water

RGO- reduced graphene oxide

EDA- ethylenediamine

°C- Celsius

eV- electron volt

a.u.- astronomical unit

nm- nanometer

cm- centimeter

CHAPTER 1

INTRODUCTION AND LITERATURE SURVEY

1.1 Semiconductors

Semiconductor devices showcase a wide range of useful properties like showing variable resistance, passing current more easily in one direction than the other and sensitivity towards light and heat. This wide range of properties is since the electrical conductivity of a semiconductor can be modified easily by adding impurities in a controlled manner or by application of electrical field or light. Semiconductor devices can be used for switching, energy conversion and amplification. The conduction of current in semiconductors happens through the movement of free electrons and holes, they are collectively called as charge carriers. The addition of impurity to a semiconductor material is known as Doping. Doping greatly increases the number of charge carriers within the semiconductors.

Semiconductor devices exhibit a diverse array of advantageous characteristics, including adjustable resistance, preferential current flow in one direction, and responsiveness to light and heat. This versatility stems from the semiconductor's capacity for facile modification of electrical conductivity, achieved through controlled addition of impurities, application of electrical fields, or exposure to light. These devices find application in switching, energy conversion, and signal amplification. Current conduction in semiconductors occurs via the movement of free electrons and holes, collectively referred to as charge carriers. The introduction of impurities into semiconductor materials, termed doping, significantly augments the population of charge carriers within the semiconductor (1).

1.2 Classification of Semiconductors

1.2.1 Intrinsic semiconductor:

An intrinsic semiconductor can be described as a material composed of highly pure semiconductor material. Essentially, it is a device wherein the quantity of electrons matches the number of holes within the conduction band. In such semiconductors, the energy gap between bands is minimal, allowing valence electrons to transition to the conduction band even at room temperature. The Fermi level of an intrinsic semiconductor resides between the valence and conduction bands, representing the energy level at which electron probability is at fifty percent. Upon application of a potential difference across an intrinsic semiconductor, electrons migrate towards the positive terminal, while holes move towards the negative terminal. The total current within a semiconductor is the aggregate of the currents attributable to free holes and electrons (2).

1.2.2 Extrinsic semiconductor:

Extrinsic semiconductors undergo a modification of their pristine state by introducing a minimal amount of impurities. These impurities, termed dopants or doping agents, serve to alter the semiconductor's properties. Dopants are typically selected based on whether they possess five electrons in their valence band (pentavalent) or three electrons (trivalent). This selection results in two distinct types of semiconductors. A semiconductor is classified as p-type when doped with impurities that generate free holes, while it is designated as n-type when predominantly hosting free electrons. Within a semiconductor crystal, numerous p- and n-type regions coexist, forming p-n junctions responsible for facilitating desirable electronic behavior (2).

1.2.2.1 Types of extrinsic semiconductors:

- **n-type semiconductor:**

Pentavalent dopants include antimony (Sb) and arsenic (As), whereas trivalent dopants include germanium (Ge) and silicon (Si). For example, four of antimony's five valence electrons establish covalent connections with germanium atoms when a little amount of antimony is introduced as an impurity into a germanium crystal, leaving the fifth electron free to move around the crystal lattice. Conductivity is increased when a potential is applied to the doped germanium crystal, causing the free electron to go in the direction of the positive terminal. This effect designates the doped crystal as an n-type semiconductor because it increases the conductivity of the crystal due to the presence of negatively charged free electrons (2).

- **P-type semiconductor:**

Three covalent connections with three Ge atoms are formed when modest amounts of trivalent dopants, such as Ge or Si, are mixed with trivalent impurities, such as aluminum, indium, or boron. As a result of electron shortage, Ge's fourth valence electron is unpaired and cannot make a covalent bond with indium. The hole that results from this electron's absence at that location indicates an area of positive charge. The semiconductor is identified as a p-type semiconductor by this configuration. A p-n junction diode is an interface made up of two types of semiconductors: p-type and n-type. This kind of diode can be used in electronic circuits as a rectifier (2).

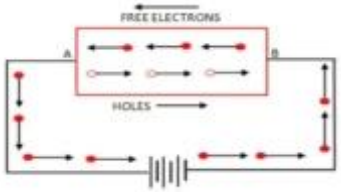

Figure 1. Schematic diagram of Intrinsic Semiconductor

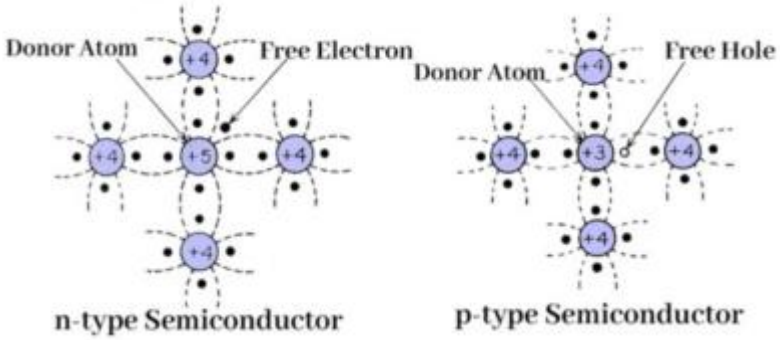

Figure 2 Schematic diagram of Extrinsic semiconductor

1.3 Doping and how it alters the property of a nanostructure in gas-sensing:

Doping plays a pivotal role in shaping the physical attributes and potential applications of diverse materials, particularly within the semiconductor realm. This assertion finds ample validation through numerous successful implementations across the semiconductor industry. Even minute quantities of impurities wield significant influence over the electrical conductivity and carrier concentration of a material.

Nanostructures boast distinctive properties dictated by their dimensions, morphology, and shape, enabling multifaceted interactions with various elements. The significance of nanostructures in commercial ventures is profound, with synthesis often involving a spectrum of metals or metal salts alongside plant extracts or organic substances. Notably, nano-sized inorganic compounds have emerged as potent antibacterial agents, leveraging their distinctive physical and chemical traits and expansive surface area to exhibit remarkable efficacy even at exceedingly low concentrations (3).

Nanoparticles have attracted attention due to their distinctive optical, mechanical, electrical, and magnetic characteristics, rendering them highly versatile materials applicable across diverse fields such as medicine and electronics. Notably, their significantly enhanced surface-to-volume ratio, in comparison to conventional counterparts, endows nanoparticles with exceptional efficacy as agents in various chemical reactions.

When noble metal dopants come into contact with Metal-Oxide Semiconductors (MOSs), a charge transfer occurs between the two, which causes the noble metal to accumulate electrons. A depletion layer forms on the metal oxide as a result of this accumulation, which balances the Fermi level. As a result, the higher initial material resistance leads to an enhanced sensing response. In addition, noble metal nanoparticles—which are well known for their remarkable catalytic activity—significantly improve oxygen molecule adsorption, which raises the concentration of oxygen ions. The direct adsorption of target gas molecules

onto the noble metal nanoparticles, followed by their migration to participate in reactions, is responsible for this increase in sensitivity and response speed. This knock-on effect significantly improves the performance of gas detection. Notably, because metal oxide-based gas sensors require very little power, there has been a significant increase in interest in room- and low-temperature sensing. The functionalization of metal oxides with noble metals lowers the temperature at which gas sensors operate (4).

Even though doping is a frequently used technique to improve sensing performance, some dopants and improper doping levels can have a negative effect on it. Excessive doping may cause doped particles to aggregate, lowering the specific surface area, active site count, and gas-sensing response efficiency of the material.

When bonded to carbon materials, metal nanoparticles such as Pt and Pd can increase gas responsiveness and accelerate gas reactions. Kim et al. combined the sol-gel technique with electrospinning to create ternary nanocomposites made of rGO/metal (Pd or Pt)-coated SnO2 nano fibers (NFs). When it came to detecting C6H6, C7H8, and CO gases, these ternary composites outperformed SnO2 and rGO/SnO2 materials in gas sensing capabilities. The sensing responses of SnO2 NFs, rGO/SnO2 NFs, and rGO/Pd/SnO2 NFs to 1 ppm C6H6 were 1.6, 3.3, and 8.3, respectively, at an operating temperature of 200 °C. Due to the high specific surface area, various heterojunctions between the materials, and the distinct sensitizing effects of Pt and Pd, the rGO/metal-co-loaded SnO2 NF sensor responds better than the original.

The characteristics of current carbon gas-sensing materials used in three major compositing systems can be outlined as follows:

1. Conductive polymers enhance both the selectivity and sensitivity of carbon materials but have relatively ow stability.
2. Metal oxides (MOSs) significantly increase the sensitivity of carbon materials, although they are hindered by long response times and poor repeatability.
3. Metal nanoparticles effectively catalyze the gas-sensing reactions of carbon materials but show poor selectivity in mixed gas environments.

Thus , it is crucial to develop a comprehensive strategy to expedite the practical the practical application of carbon materials in resistive gas sensors.

1.4 Stability and reusability of doped nanostructure in gas-sensing

Gas sensors play a crucial role in preserving environmental safety. For the protection of the environment and public health, monitoring and regulation of gas levels are essential. In order to prevent potentially fatal circumstances, gas sensors are essential for detecting dangerous gases such as carbon monoxide (CO), carbon dioxide (CO2), and nitrogen dioxide (NO2). Preventive detection is essential for saving human lives. Furthermore, gas sensors play a critical role in environmental conservation by tracking emissions from a variety of sources, including transportation and industrial activities, to guarantee that environmental laws are followed and to lessen the harm that emissions do to ecosystems (5).

One of the main causes of air pollution nowadays are volatile organic compounds (VOCs), which present serious environmental problems. VOCs combine with other gases in the presence of sunshine to create ground-level smog compounds, which can damage plants, impede the formation of seeds, and impede fertilization. Long-term exposure to volatile organic compounds (VOCs) in humans can cause major health problems such lung cancer, strokes, and chronic obstructive pulmonary disease. The World Health Organization (WHO) estimates that the combined impacts of indoor and outdoor air pollution cause about 7 million premature deaths each year, and that by 2050, this number will have doubled (6).

Materials used in gas sensing devices include semiconductors (like Si, GaAs, GaN, and ZnS), metals (like Pd, Pt, Ag, and Ni), ionic compounds (like CaF2, Ag2S, and Na2CO3), and polymers (like poly ether, polyurethane, and Nafion). These materials do, however, have a number of disadvantages, including low selectivity, extended drift, hazardous exposure, and the requirement for sophisticated technology. Furthermore, in complicated situations, sensing may become more difficult due to interference from other gases. A gas sensor needs to have a long life cycle, good selectivity, dependability, low detection limits, outstanding repeatability, and high sensitivity in order to function well. The creation of materials with a greater surface-to-volume ratio is necessary to improve sensor performance since it will enable the testing gas to interact with the active layer and affect its behavior more effectively (6).

It is essential to comprehend their gas-sensing methods and choose suitable gas-sensing materials in order to produce high-performance resistive gas sensors. Target gas adsorption, electron transport, and chemical reaction rates are all dependent on the physical and chemical characteristics of these materials, including their size, shape, crystallinity, specific surface area, and active site concentration. The performance of gas sensors is influenced by all of these variables combined. One-dimensional (1-D) nanomaterials have attracted a lot of attention from scientists lately because of their high length-to-diameter ratios, many exposed active sites, and enormous surface areas. Resistive gas sensors' sensitivity and response time are greatly increased by these properties, which also enable quick charge transfer and effective gas-sensitive responses (7).

1.5 Different methods of synthesizing nanostructures

Semiconductor materials are crucial for various applications, largely due to their narrower band gaps. However, if a semiconductor material has a large band gap, it can lead to a high electron-hole recombination rate, which poses a challenge. To address this issue, synthesis methods are essential for reducing band gaps and improving the material's performance.

Such methods include:

a. Hydrothermal synthesis

b. Solvothermal synthesis

c. Microemulsion

d. Sol-gel method

e. Microwave synthesis

f. Physical Vapor deposition

g. Chemical Vapor deposition

(a) HYDROTHERMAL METHOD

The term "hydrothermal" refers to the crystallization process used in the hydrothermal synthesis method, which usually requires high vapor pressure and a heated aqueous solution. A Hydrothermal Autoclave Reactor is a piece of specialized equipment needed for this type of nanoparticle manufacturing. This reactor is a sturdy vessel built to tolerate high internal pressures and temperatures.

The autoclave reactor can withstand high heat and pressure safely and consistently for lengthy periods of time thanks to its thick, steel-walked cylindrical vessels and hermetic sealing. The autoclave's material has to be solvent-resistant. The "closure" is the most important portion of the hydrothermal autoclave reactor, however seals are also quite important.

Special protective coatings are used to stop corrosion because many hydrothermal processes utilize solutions that can damage the autoclave's inside. These coatings can be used to cover certain areas of the autoclave's interior or the entire thing, fitting in with ease (8).

Advantages of Hydrothermal Synthesis Method for Nanoparticle Synthesis

1. Capable of securely producing crystalline phases that become unstable at higher temperatures.

2. As a material approaches its melting point, it grows materials that are known to have a higher vapour pressure.

3. Produces superior quality, larger-sized crystals and nanoparticles, allowing for customization of their composition and content.

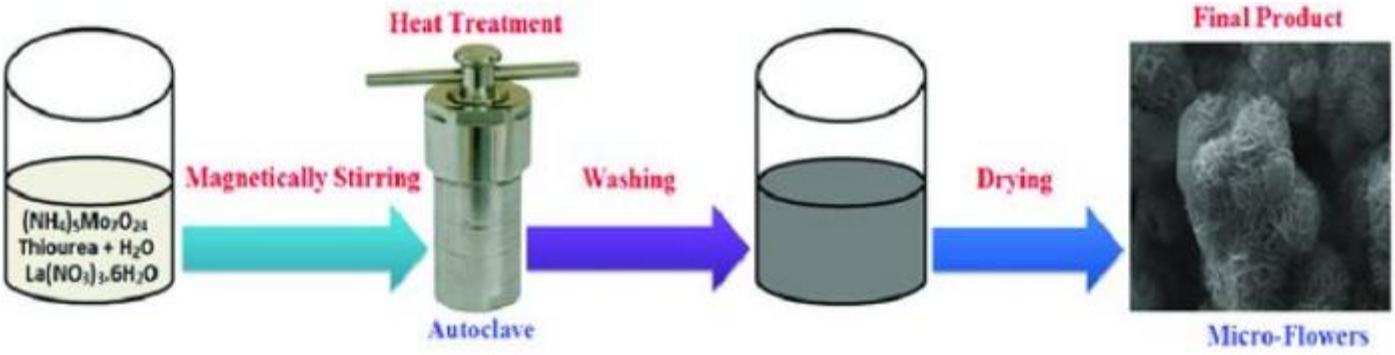

Figure 3 Schematic diagram of Hydrothermal Synthesis Method

(b) SOLVOTHERMAL SYNTHESIS

With the exception of using less energy to directly convert algal biomass into biofuels, this method is comparable to the hydrothermal process. The use of a solvent is the primary distinction between solvothermal and hydrothermal processes. The solvent in the hydrothermal technique is only water. Other than this, the solvothermal method's processing parameters and experimental setup are identical to those of the hydrothermal process

.

Figure 4 Schematic diagram of Solvothermal Synthesis

(c) Microemulsion technique

The synthesis of nanoparticles through the microemulsion method has garnered significant attention in current research. Since the discovery of microemulsions, they have become increasingly important in both fundamental scientific inquiry and various industrial applications. Their unique characteristics—such as their huge interfacial area, ultralow interfacial tension, thermodynamic stability, and ability to solubilize otherwise immiscible liquids—account for this.

The creation of nanoparticles can be made more versatile by using the microemulsion process, which allows for greater control over the size, shape, morphology, homogeneity, and surface area of the particles. Reactant exchange happens during this phase when the microemulsion precursors are mixed and the water droplets collide. This exchange occurs quickly enough to support particle coagulation, simultaneous nucleation growth, and the precipitation reaction. The intended nanoparticles are then produced, frequently encircled by stabilizers, surfactants, or water droplets.

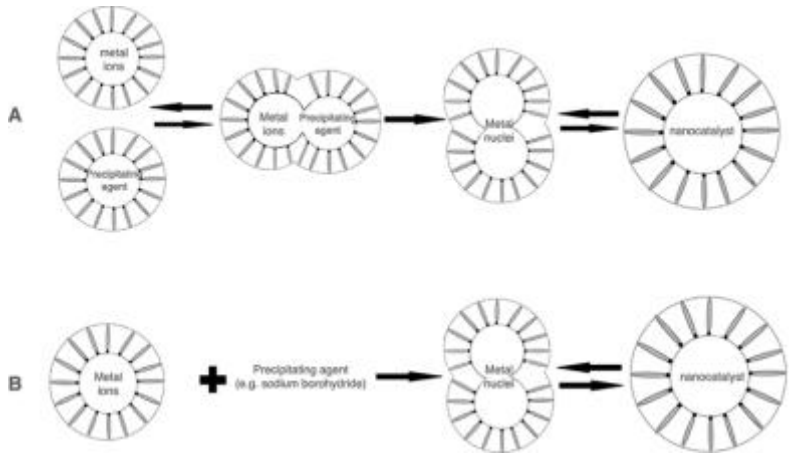

Figure 5 Schematic diagram of microemulsion techniques

(d) Sol-gel method

For the creation of nanoparticles, this wet chemical technique is extensively used in the domains of material sciences and ceramic engineering. Three phases are usually involved in the sol-gel process:

1. The development of gel in a solution containing colloidal particles.

2. Nitrate or alkoxide precursor hydrolysis and polycondensation, frequently including hypercritical gel drying.

3. Additional alkoxide precursor hydrolysis and polycondensation, then aging and drying at ideal pressure and temperature levels.

Solid particles with diameters ranging from 1 to 100 nm are known as colloids, and the particles scattered in the aqueous solution are called sols. The capacity of the sol-gel method to create several physical shapes of a material with the same composition by altering the experimental circumstances is one of its main benefits.

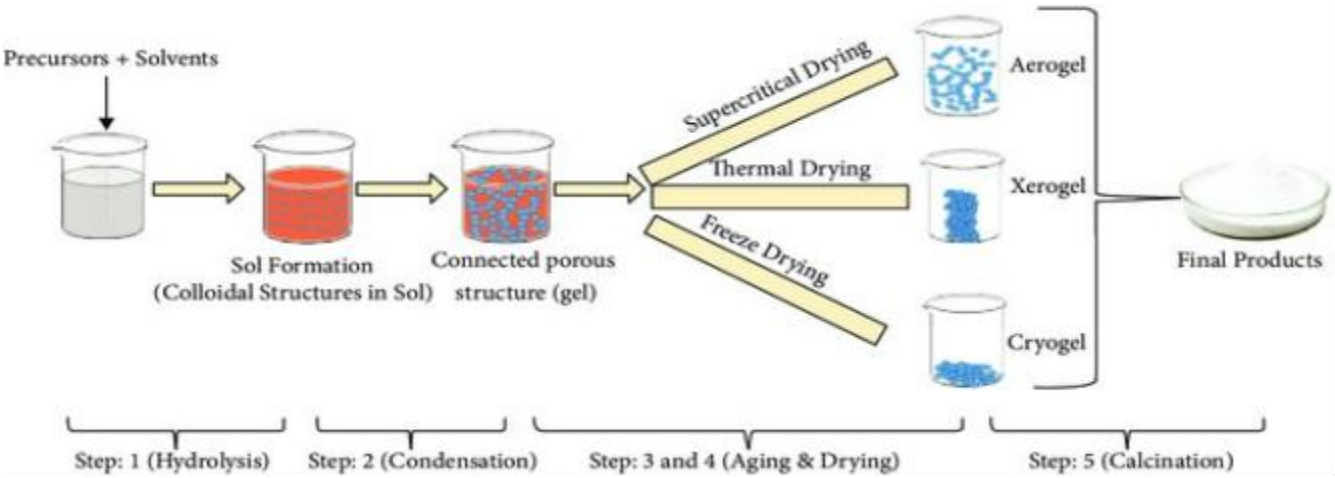

Figure 6 Schematic diagram of Sol-gel method

(e) MICROWAVE SYNTHESIS

An increasing amount of research is pointing to the use of microwave energy for material development in a variety of applications and industrial processes. During interaction, the absorption process primarily generates heat energy within the material. Microwaves are utilized to heat both matter and form. Under certain experimental conditions, plasmas can be generated by exciting gases via microwaves, aiding in material processing.

In bulk form, metals typically do not absorb microwave energy and act as excellent reflectors. Other materials, depending on their composition, temperature, and structure, may absorb or reflect microwave energy.

Numerous benefits come with using the microwave process, such as low cost, accurate and controlled heating, quick processing periods, fewer harmful emissions, large product yields, and environmental friendliness.

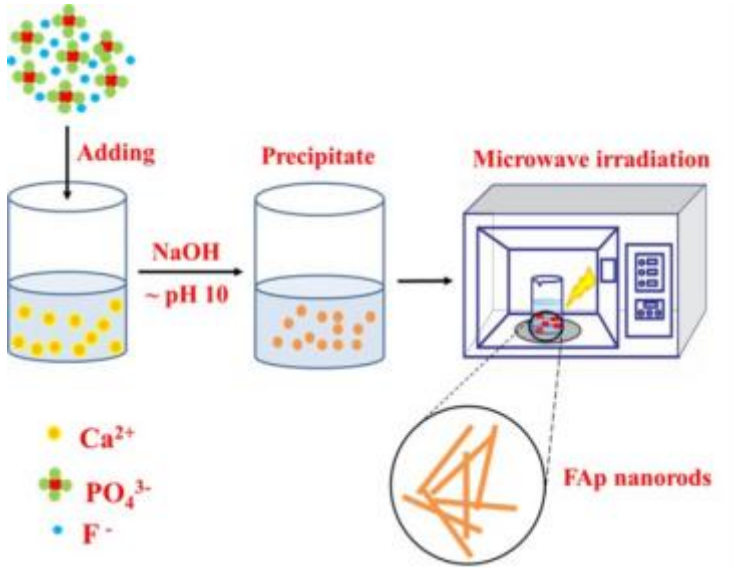

Figure 7 Schematic diagram of microwave synthesis

(f) Physical Vapor Deposition

In physical vapor deposition (PVD), a thin layer of material is deposited in a vacuum environment onto a substrate surface. Magnetron sputtering, electron beam sputtering, ion-plating, and sputtering are some of the various forms of PVD processes.

In these procedures, an inert gas, such as argon (Ar), and a high-energy ion source are used to remove atoms from a target material while a vacuum is maintained. A high-energy source is applied to the target material, vaporizing the atoms on its surface. Then, inside the deposition chamber, these vaporized atoms travel in the direction of the substrate surface.

When a metal-oxide or carbide is deposited, the reaction takes place, which speeds up the deposition process. The atoms that have been vaporized are deposited as a thin layer on the substrate surface.

This method is flexible and can be applied to substrates to deposit layers of different inorganic and some organic compounds.

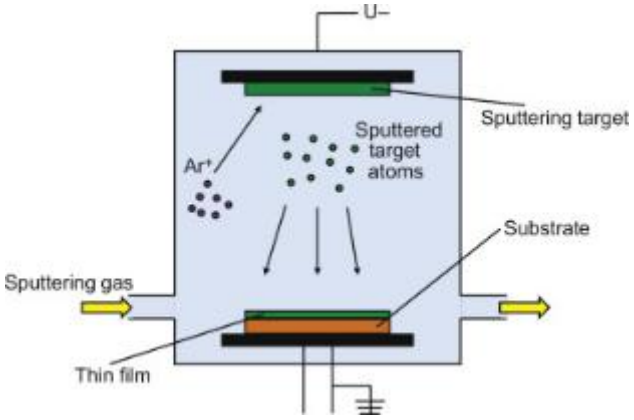

Figure 8 Schematic diagram of physical vapor deposition

(g) Chemical Vapor Deposition

This process can also be used to deposit thin films. The primary difference between PVD and CVD is the target material's physical state: in PVD, the target is solid, whereas in CVD, the target is gaseous.

High purity, density, and strength materials are produced by CVD methods, which makes them advantageous for the ceramic and semiconductor sectors. This heat-sensitive technique is frequently used in the production of nanomaterials in the presence of metal catalysts.

Materials are created in CVD by reacting chemical constituents in the vapor phase on a heated substrate. Heat, radiation, or plasma are examples of high-energy sources that can activate the target material. The gaseous ingredients are then transported to the hot substrate and deposited there using a carrier gas, such as N2 or H2.

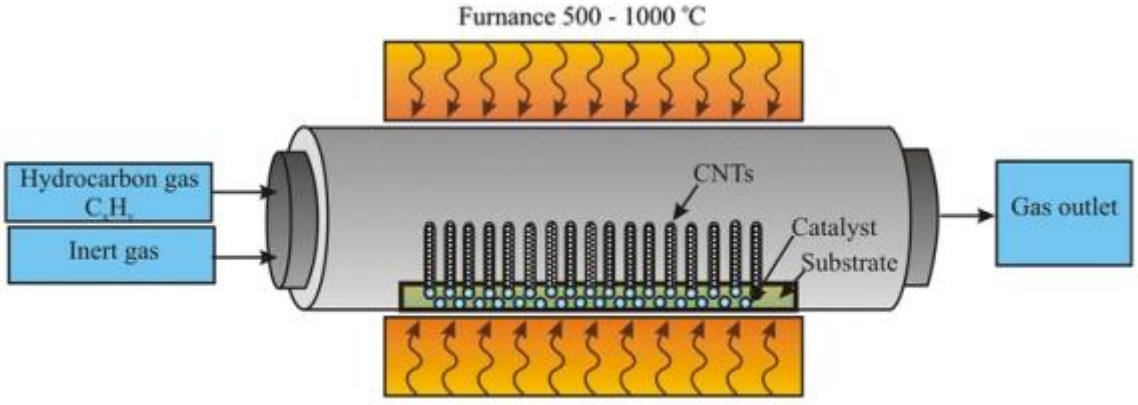

Figure 9 Schematic diagram of chemical vapor deposition

1.6 Volatile Organic Compounds and their Environmental Effects:

1.6.1 Volatile Organic Compounds (VOCs)

Volatile Organic Compounds (VOCs) are organic chemical substances found in a wide range of products that, in typical circumstances, easily evaporate and spread throughout the environment. Because of their increased volatility, mobility, and resistance to degradation, volatile organic compounds (VOCs) can travel great distances in the environment. Aromatic hydrocarbons like toluene, xylene, and benzene as well as halogenated hydrocarbons like trichloroethylene and chloroethylene are typical examples of volatile organic compounds (VOCs). Taking a bath, eating, drinking water, swimming, and other activities that involve contaminated water sources can all result in contact with volatile organic compounds (VOCs).

Volatile organic compounds (VOCs) come from man-made and natural sources. Anthropogenic sources include home and industrial activities like food extraction, septic systems, petroleum storage, and the pharmaceutical industry, whereas natural sources include emissions from plants and forest fires.

VOCs are classified as greenhouse gases because they have the ability to absorb Earth's radiation. The rise in their atmospheric concentration is linked to global warming. VOC emissions in the pharmaceutical industry are caused by the use of organic solvents in chemical synthesis processes, such as xylene, isopropyl alcohol, ethanol, and toluene.

Reducing the amount of volatile organic compounds (VOCs) in the environment requires efficient technology. Traditional techniques for reducing volatile organic compounds (VOCs) include chemical oxidation, burning, biological oxidation, and the adsorption of different carbon materials. The use of nanomaterials to reduce environmental pollution is one of the major trends in VOC reduction (9).

1.6.2 Classification of VOCs:

VOCs can harm the human and environmental health. They evaporate at normal pressure and room temperature making them present in both open and closed spaces. Some VOCs are more volatile than others, making them more dangerous to human and environmental health (10).

Table [1] depicts the classification of VOCs based on their volatile characteristics.

Class	Examples of Compounds	Boiling Point Range °C
Very volatile organic compounds (VVOCs)	propane, butane, methyl-chloride	0 to 50–100
Volatile organic compounds (VOCs)	formaldehyde, toluene, acetone, isopropyl alcohol	50–100 to 240–260
Semi volatile organic compounds (SVOCs)	pesticides (chlordane, DDT), plasticizers (phthalates)	240–260 to 380–400

1.6.3 Impact of VOCs on Human and Environmental Health

VOCs have various impacts on the health of humans and the environment through carcinogenicity, stratospheric ozone depletion, damage to materials, global climate change, etc. Air pollution has become a serious public health issue. Harmful effects from exposure to VOCs result in different reactions and interactions in the human body. There is a chemical diversity of VOCs which causes adverse effects on human health. The effects caused by VOCs include irritation, allergic effects, and sensory, respiratory, and carcinogenic effects. VOCs play a major role in global warming by absorbing infrared radiation from the surface of the earth. VOCs cause a change in the concentration of the ozone layer, which is a strong greenhouse gas leading to global warming.

Aerosol nucleation is thought to be facilitated by the organic acids produced when volatile organic compounds (VOCs) oxidize. Car exhaust that contains aromatic volatile organic compounds (VOCs) is photo oxidized, producing a large amount of precursors that allow ultrafine particles to form and develop in the atmosphere. Certain volatile organic compounds possess a distinct smell, the strength of which can be described in terms of an odour threshold, which is the concentration at which 50% of the population is unable to detect the odor. Practical measurements should be used to determine the odor threshold that the VOCs mixture emits.

To prevent exposure to volatile organic compounds (VOCs), gas sensors can be used to measure high VOC concentrations and assess the quality of the air (11).

Chapter 2

Synthesis Methods for Nano-structures - ZnA & ZnC

2.1 Synthesis of $Ag@SnO_2$ Nanostructures:

The desired concentration of $SnCl_2.2H_2O$ (0.01M) were mixed with ethanol and distilled water using that are present in ratio of 1:1 on magnetic stirrer for 30mins. In our study we have taken, 50ml of double distilled water and to this a mixture of 2.83g $SnCl_2.2H_2O$ and 0.17g $AgNO_3$ was added and 0.5g of NaOH was added to reaction mixture with constant stirring for 30mins. The mixture was then transferred into a 100ml of Teflon and heated at 160°C for 8h. After letting the mixture cool down naturally to room temperature, Centrifugation of obtained product was done followed by washing it with water and drying at 60°C for 12hrs. Finally, Ag/SnO_2 nanocomposite was obtained and stored in viel (12).

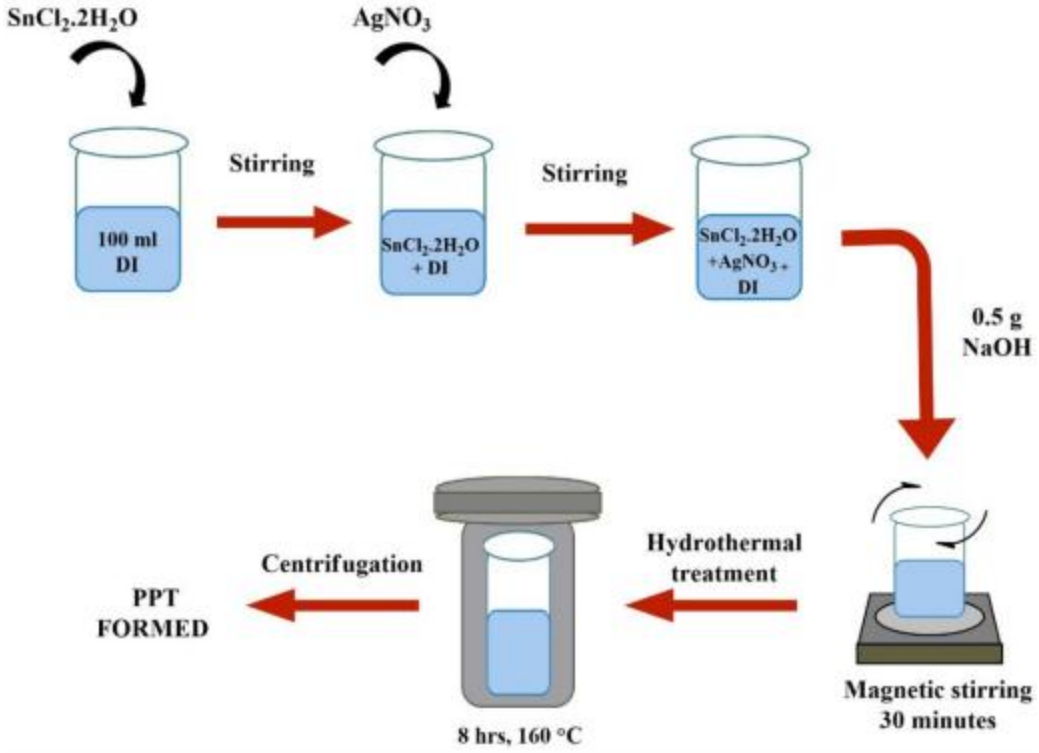

Figure 10. Systematic diagram of synthesis of $Ag@Sn0_2$ (ZnA) nanocomposite

2.2 Synthesis of g-C_3N_4

Synthesizing of g-C_3N_4 requires, 15g Urea was added in a thermoflask that was placed in muffle furnace for 2hrs at temperature 550°C at a rate of 5°C/min

2.3 Synthesis of $Ag@SnO_2$/g-C_3N_4 nanocomposite:

The prepared 0.18g g-C_3N_4 was mixed with 18ml of distilled water and underwent sonification for 120min in order to get homogenous dispersion. A solution was formed by dissolving 2.83g $SnCl_2.2H_2O$ and 0.17g $AgNO_3$ in 30ml DI. This obtained mixture was

added gradually to homogenous dispersion and was stirred for 1hr on magnetic stirrer. Then, 2.11g Sodium Carbonate was dissolved in 5ml DI dropwise and stirred until gel like consistency is observed. The mixture was then transferred to Teflon and heated at 150°C for 12hrs. The resulted precipitation was centrifuged followed by washing with water for several times and air dried to obtain the $Ag@SnO_2/g\text{-}C_3N_4$ nanocomposite (13).

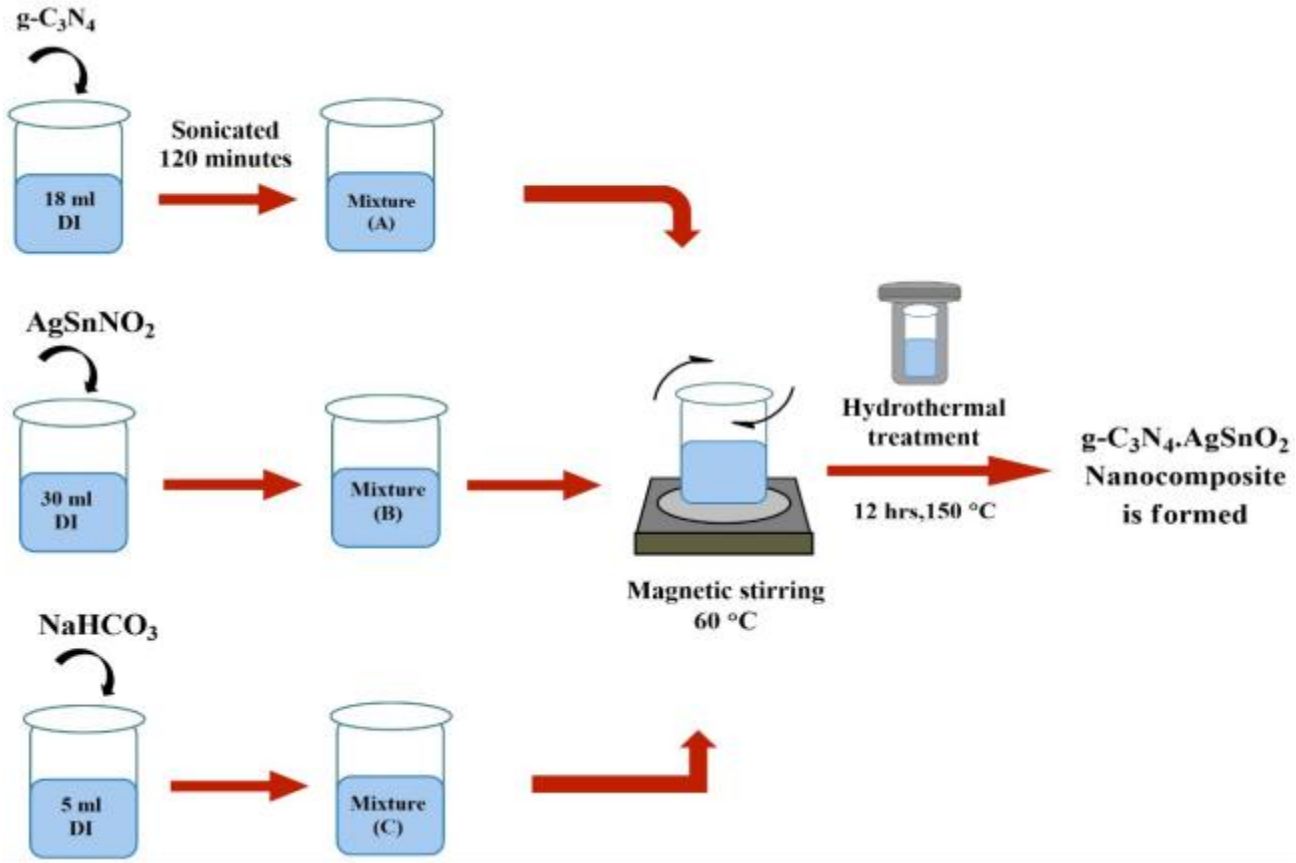

Fig 11. Systematic diagram of synthesis of $A@Sn0_2/g\text{-}C_3N_4$ nanocomposite

Chapter 3

Characterization Techniques and Fabrication Methods

3.1 Standard Characterization Techniques

3.1.1 XRD (X-ray diffraction)

The X-ray diffraction (XRD) technique is widely employed in nanotechnology to accurately characterize the composition, crystal structure, and crystalline grain size of nanoparticles. XRD operates on the principle of X-ray scattering, which occurs when X-rays strike nanoparticles, causing the electrons in the atoms' nuclei to revolve. This interaction results in the scattering of X-rays in different directions, creating interference patterns. Among these patterns, only those resulting from constructive interference lead to diffraction.

The four primary parts of standard powder XRD equipment are the receiving optics, X-ray detector, specimen stage, and X-ray source. The sample stage is located in the middle of the focusing circle, with the source, detector, and related optics situated on its periphery. XRD analysis is based on Bragg's law. This law enables precise quantification of experimental findings for the identification of crystal structures. Bragg's angle, theta, is the angle formed by the plane of the specimen and the X-ray source; the angle formed by the X-ray projection and the detector is 2tetha (14).

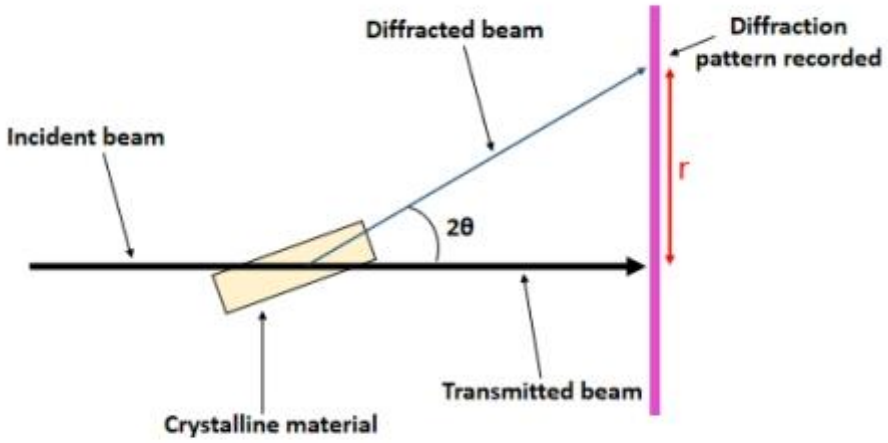

Figure 12. Schematic diagram of X-Ray Diffraction

3.1.2 SEM/EDX Analysis:

Using a convergent electron beam that interacts with the atoms of the sample materials, SEM scans and creates images of the surfaces of materials. Several signals are produced by the method, which can be used to determine surface topology and material composition. Applying a high-energy electron beam (100–30,000 eV) that is released from a heat source is part of the SEM's operating mechanism.

SEM generates high-resolution, high-magnification images by directing a focused electron beam onto a sample, producing measurable electron energies. These are analyzed to create a three-dimensional image. The electron beam also generates X-rays, which the Energy Dispersive X-ray (EDX) instrument collects and converts into data. The EDX output is a spectrum showing the frequency of X-ray reception at each energy level, with peaks unique to each element. Higher peaks indicate higher element concentrations, and overlapping peaks from mixtures are resolved using specialized software (15).

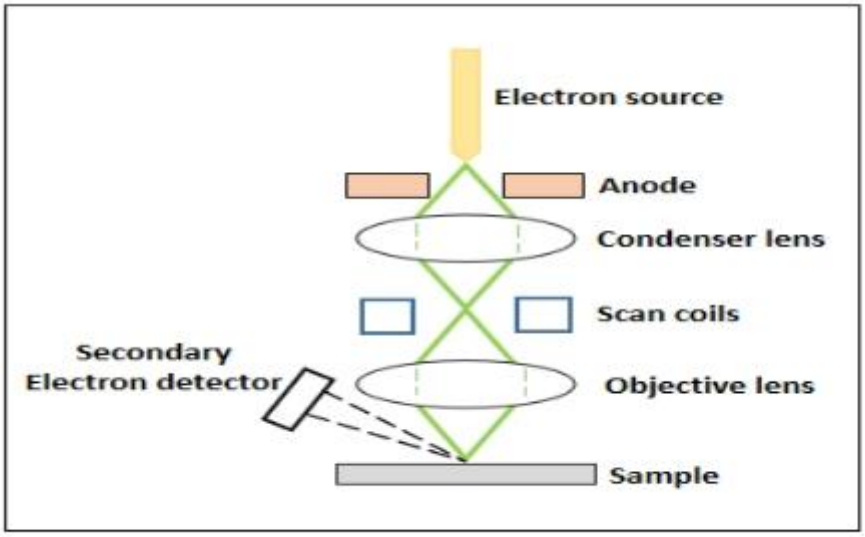

Figure 13. Schematic diagram of Scanning Electron Microscope

3.1.3 Raman Spectroscopy

Raman spectroscopy is a highly valuable tool for analyzing two-dimensional (2D) materials. The effectiveness of Raman spectroscopy relies on the polarizability of a bond, which measures how easily the bond can be deformed in an electric field. This depends on the ease with which electrons in the bond can be displaced, creating a temporary dipole. Bonds with a high concentration of loosely held electrons exhibit greater polarizability, resulting in an intense Raman signal. Consequently, Raman spectroscopy is typically more sensitive to the overall molecular structure rather than specific functional groups, unlike infrared (IR) spectroscopy. Analyzing both organic and inorganic chemical species is possible with Raman spectroscopy. Raman activity is frequently observed in atoms with numerous electrons, such as metals in coordination compounds, since these atoms have loosely bonded

electrons. By providing details on metal-ligand connections, this method sheds light on the stability, composition, and structure of these complexes.

A typical Raman instrument consists of three main elements. The first equipment to be installed is the illumination system, which typically consists of one or more lasers that must emit light at a frequency that is incompatible with the solvent and sample. The sample illumination system, which determines the phase of the substance being studied, comes in second and differs based on whether the instrument is a standard macro-Raman or has micro-Raman capabilities. In order to evaluate the scattered light, the spectrometer—which is typically positioned 90 degrees from the incident light—often has filters or a monochromator.

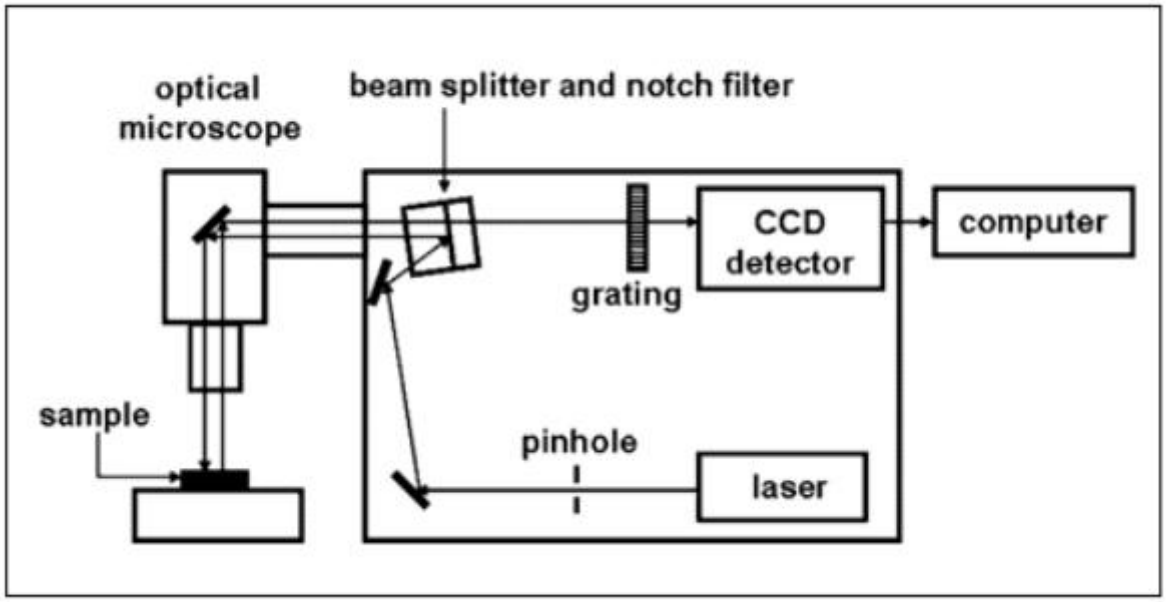

Figure 14. Schematic diagram of Raman Spectroscopy

3.1.4 UV- Visible Spectroscopy

UV-Vis spectroscopy is an analytical technique that compares a sample to a reference or blank sample to determine how much of a given wavelength of UV or visible light a sample absorbs or transmits. This measurement provides information on the components and their concentrations in the sample, depending on its composition.

The equipment used in UV-visible spectroscopy consists of a stable light source with a wide range of wavelengths of emission, usually a xenon lamp. A monochromator rotates to pick the desired wavelength, dividing light into a small range of wavelengths. It is often based on diffraction gratings. The sample is then exposed to the chosen light. For an accurate analysis, it is important to measure a reference or "blank" sample, like a cuvette filled with solvent. Light is converted into a readable electrical signal by a detector after it has passed through the sample. This detector is frequently based on photoelectric coatings or semiconductors.

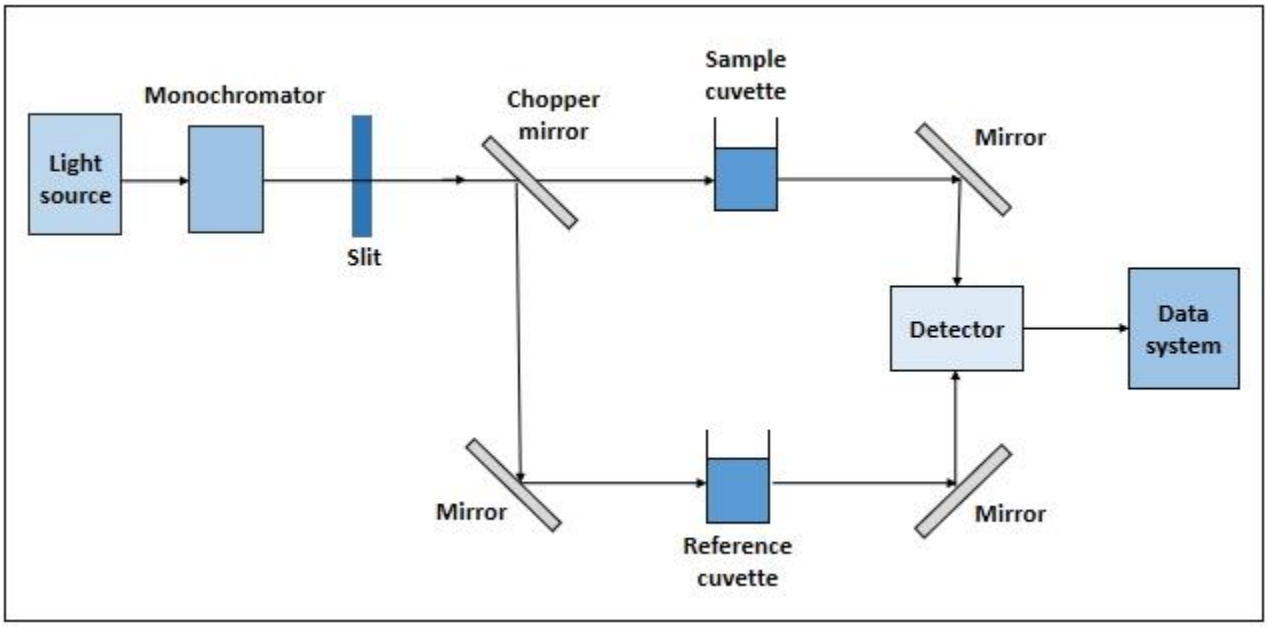

Figure 15. Schematic Diagram of UV-visible spectrophotometer

3.1.5 FTIR

For analyzing nanoparticle surfaces, figuring out their chemical makeup, and locating reactive surface locations, FTIR is a flexible technique. By separating distinctive functional groups from spectral bands, this method makes the conjugation of nanomaterials and adsorbed biomolecules visible. The vibrational frequencies of the atomic bonds in the nanoparticles are represented by absorption peaks in the FTIR spectrum. Peak intensity in FTIR directly indicates the type of substance present, making it an excellent tool for qualitative study.

A sample is exposed to an infrared radiation beam, and the FTIR method measures variations in the radiation's wavelength and intensity. The material specimen may manifest as a solid, liquid, or gas. An infrared source, like a thermal or laser source, produces the beam of radiation, which a beam splitter divides into two beams. While the other beam goes through a reference, the first beam goes through the sample. After that, a second beam splitter recombines the two beams and sends them to a detector, like a thermocouple or photodiode. The difference in phase and amplitude between the two beams determines the interference pattern that the detector measures.

The material specimen could take the form of a gas, liquid, or solid. The radiation beam is produced by an infrared source, similar to a thermal or laser source, and splits into two beams using a beam splitter. The first beam passes through the sample and the other beam passes through a reference. The two beams are then recombined by a second beam splitter and sent to a detector, such as a thermocouple or photodiode. The interference pattern that the detector observes is determined by the phase and amplitude difference between the two beams.

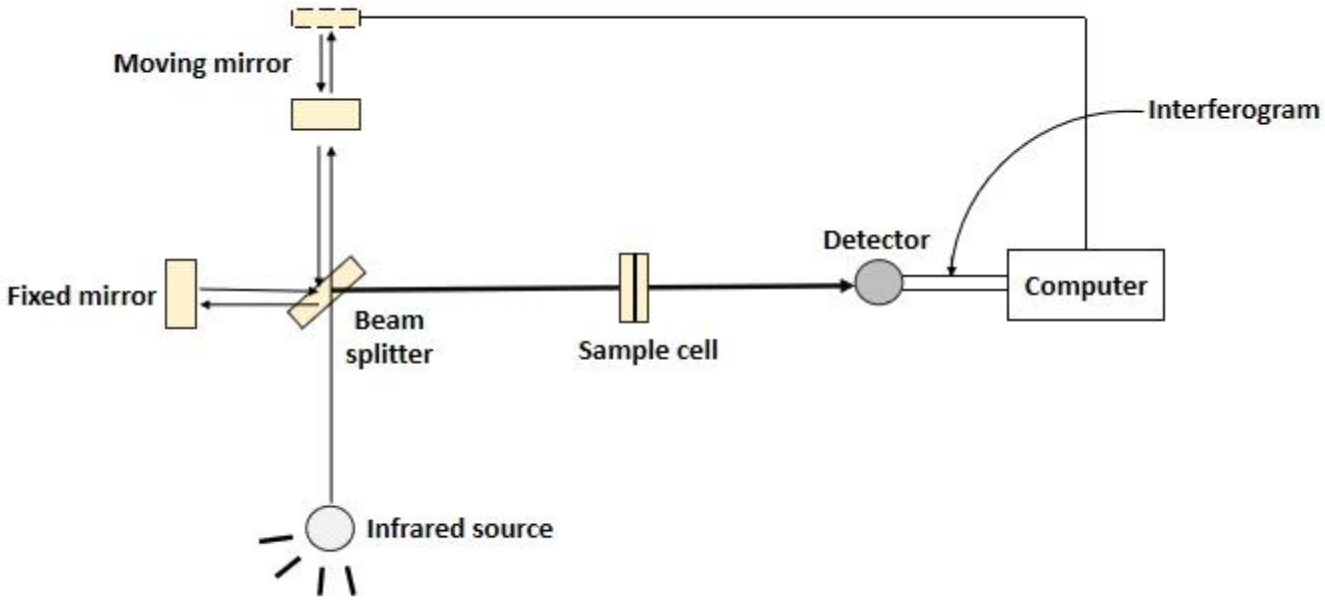

Figure 16. Schematic Diagram of Fourier Transform Infrared Spectroscopy

CHAPTER 4

RESULT AND DISCUSSION

4.1. X-Ray Diffraction Analysis

X-ray Diffraction (XRD) patterns were utilized to assess the phase purity and confirm the successful synthesis of Ag@SnO2/g-C3N4 and Ag@SnO2 (white powder), as illustrated in Figure 17 with an inset graph in Figure 18. However, the Ag peaks were not distinctly detected, possibly due to the low concentration of Ag or overlapping peaks with SnO2 in the range of 20-27°. The presence of diffraction peaks corresponding to Ag confirms the successful attachment of Ag to the Ag@SnO2/g-C3N4 nanostructures.

Distinct diffraction peaks observed at 13.1° and 27.5° correspond to the (100) and (110) planes of g-C3N4, respectively, as demonstrated in Figure 19. These peaks likely originate from the interplanar spacing of the tris-triazine unit and the conjugated aromatic system, respectively.

Additional diffraction peaks at 26.6°, 33.9°, 51.7°, and 65.9° correspond to the (110), (101), (211), and (301) planes of tetragonal rutile SnO2, respectively.

A peak observed at 27.8° is attributed to the anchoring of Ag nanoparticles. This occurrence suggests that the addition of Ag enhances the crystallinity of the material, resulting in a stronger matching peak for g-C3N4, even at low concentrations.

.

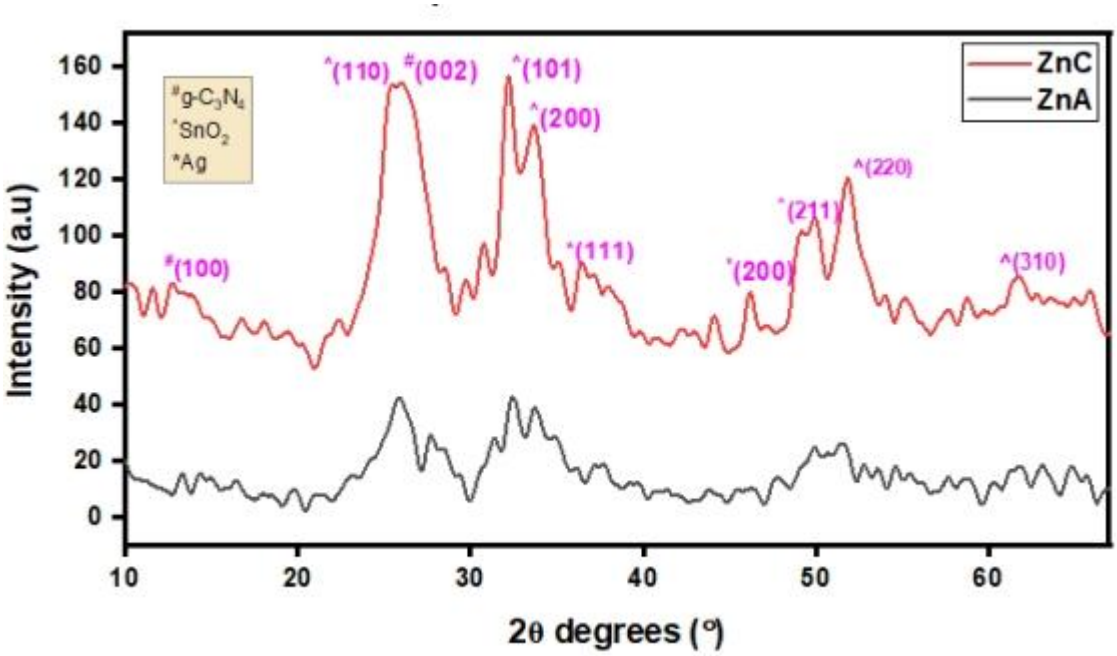

Figure 17. XRD pattern of ZnA and ZnC

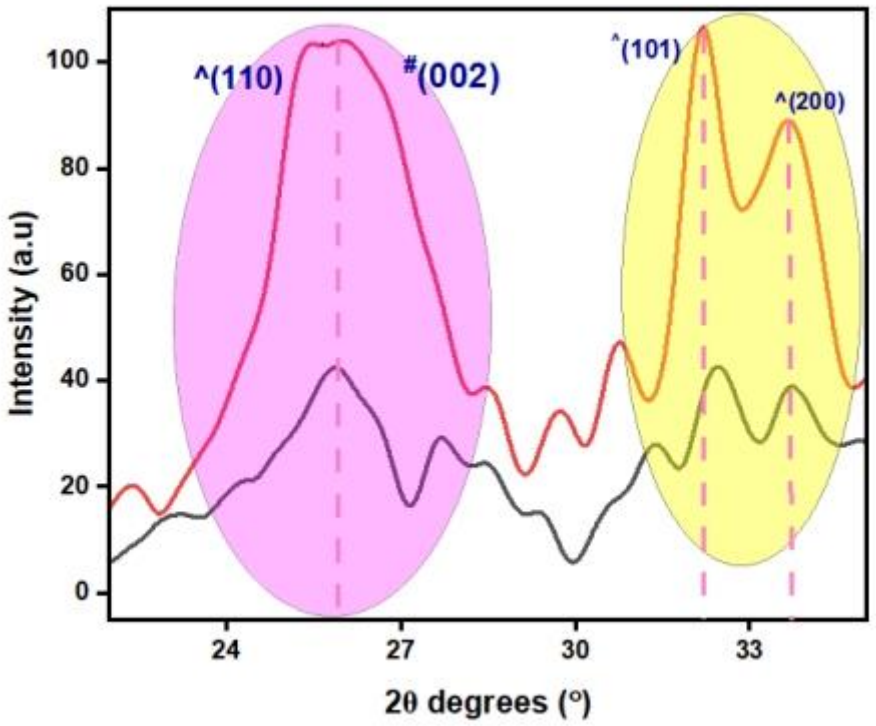

Figure 18. Inset graph of ZnA and ZnC

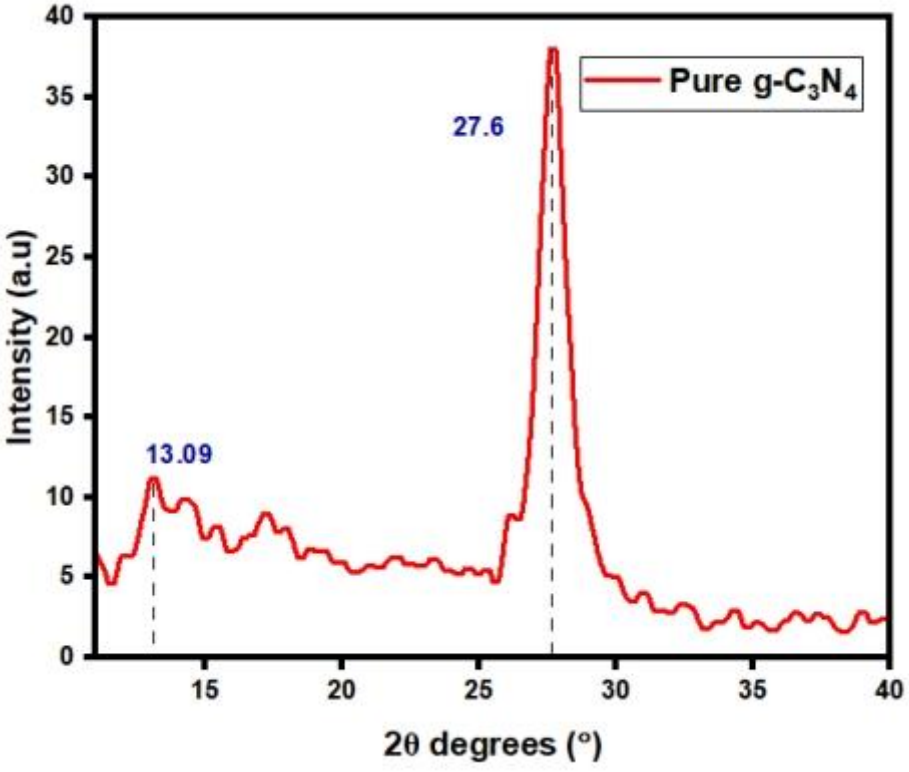

Figure 19. XRD pattern of prepared g-C_3N_4

4.2 Morphology:

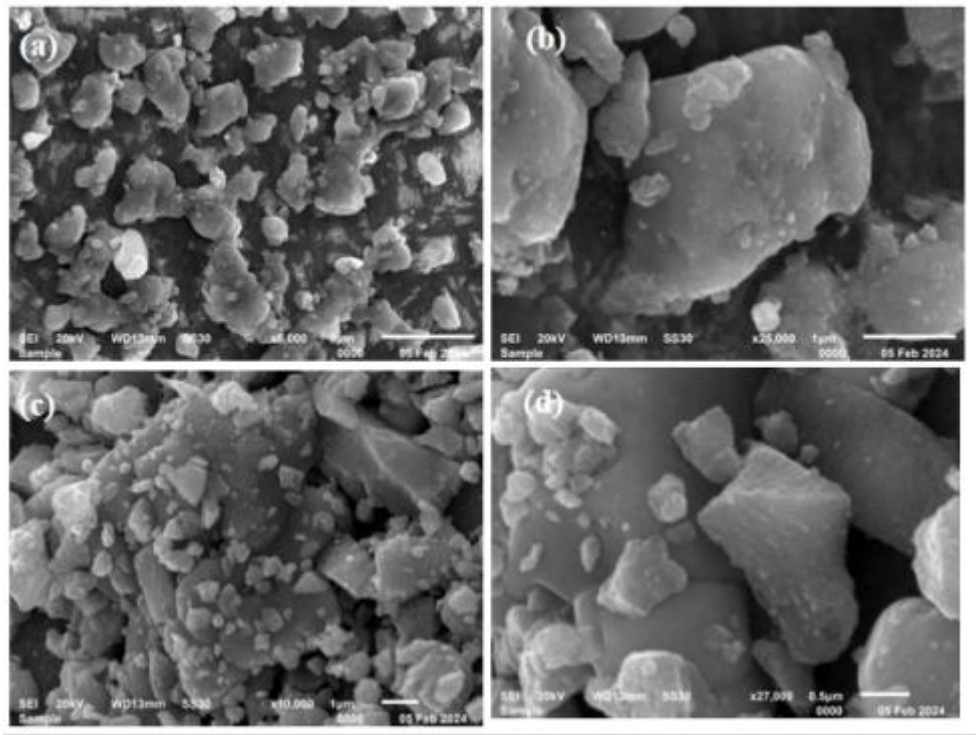

Figure 20. SEM images of ZnA and ZnC

Figure 20 shows the Scanning electron microscopic images of Ag@SnO_2 and Ag@SnO_2/g-C_3N_4. The images of Ag@SnO_2/g-C_3N_4 displayed uniform distribution of tiny nanostructures over the scanned surface with a sheet-like structure. SnO_2/g-C_3N_4 sheets in the hybrid nanostructure were decorated with spherical Ag nanoparticles. SEM images of Ag@SnO_2 and the Ag@SnO_2/g-C_3N_4 nanostructures further suggested that Ag were decorated uniformly over the SnO_2 and g-C_3N_4 sheets, respectively. Further, EDAX analysis in Figure 21 demonstrated the synthesis of Ag@SnO_2 with a single phase and great purity for both Ag@SnO_2 and the Ag@SnO_2/g-C_3N_4 under the given conditions.

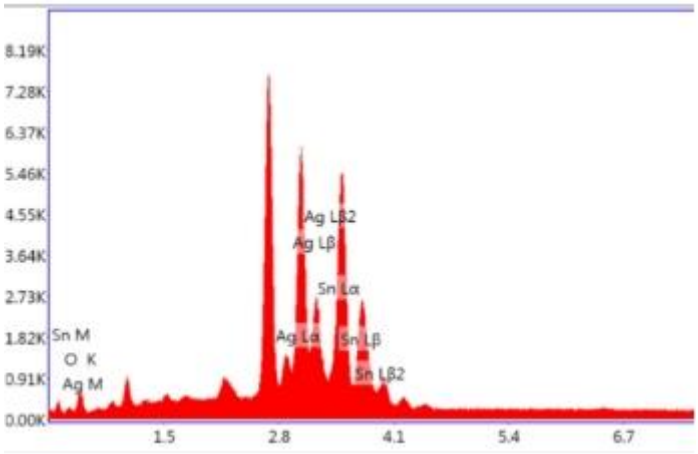

(A)

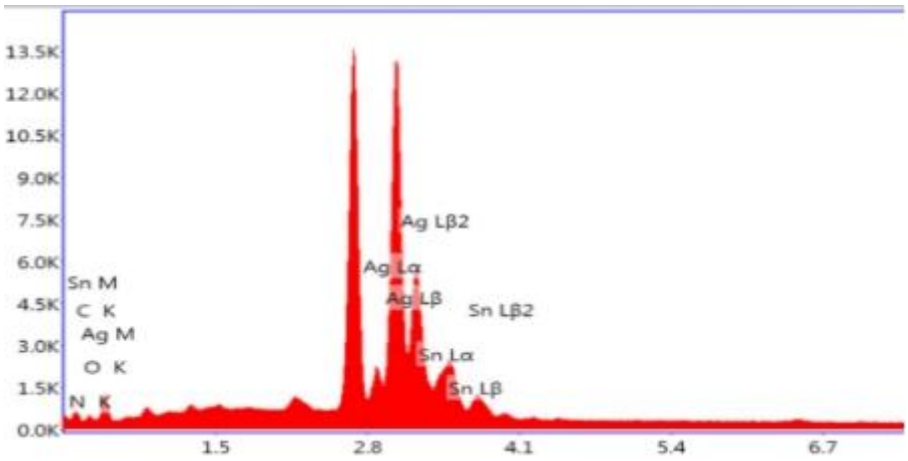

(B)

Figure21. (A) and (B) showing EDX data for ZnA and ZnC

Element	Weight %	Atomic %
O K	7.06	35.13
AgL	37.97	28.01
SnL	54.97	36.86
C K	3.22	14.36
N K	0	0.01

(C)

Figure22. (C) showing EDX table with weight (%) and atomic (%)

The Brunauer-Emmett-Teller (BET) method was used to study the surface properties of the nanostructures as surface features of the material play a crucial role in gas sensing. Adsorption-desorption and pore size distribution curves are represented in Figure 23. The $Ag@SnO_2/g\text{-}C_3N_4$ has a larger surface area as compared to $Ag@SnO_2$ and shows mesoporous properties. The surface area, pore size, and pore volume of $Ag@SnO_2$ and $Ag@SnO_2/@g\text{-}C_3N_4$ has been calculated and tabulated in table 2.

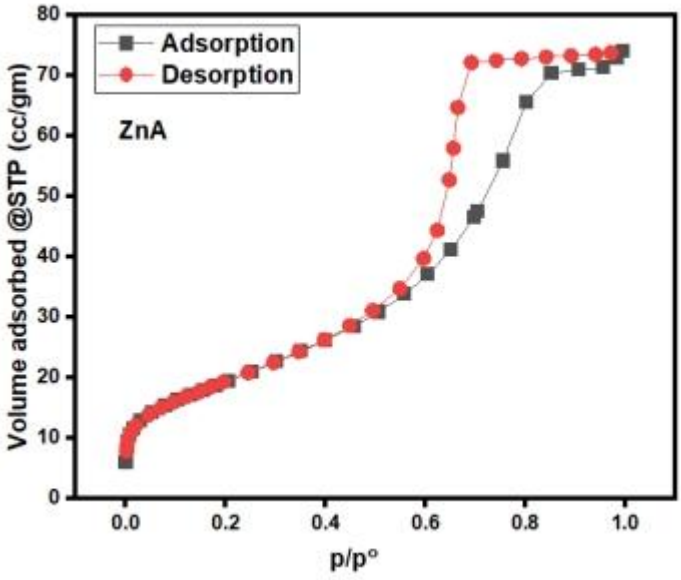

(a)

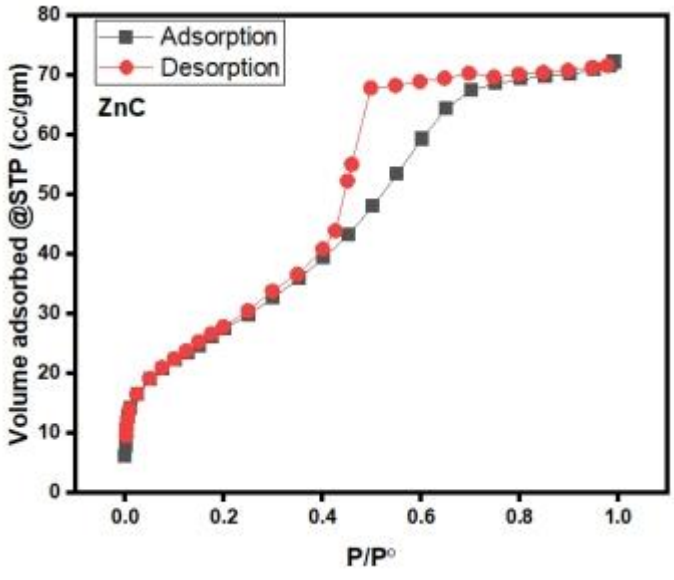

(b)

Figure 23.. Adsorption-desorption curve of (a) ZnA and (b) ZnC using BET

Parameters	$Ag@SnO_2$	$Ag@SnO_2/@g\text{-}C_3N_4$
Pore size (cm)	6.38×10^{-7}	4.26×10^{-7}
Surface area (cm^2/g)	71.3×10^4	104.6×10^4
Pore volume (cm^3/g)	0.1139	0.1115

Table2 : showing pore size (cm), surface area (cm) and pore volume (cm) of ZnA and ZnC nanocomposites

4.3 Optical Analysis:

Figure 24 depicts the UV-visible spectra of $Ag@SnO_2$ and $Ag@SnO_2/g\text{-}C_3N_4$ nanostructures. The absorption band of ZnC is observed in the visible range at 302 nm, while the absorption band of pure SnO_2 is detected at 388 nm, approaching the visible zone (according to literature values). The hybrids of ZnC and ZnA exhibit absorption at 302.4 nm and 284.4 nm, respectively.

However, the data clearly demonstrate that the $SnO_2@C_3N_4$ nanostructures exhibit an absorption edge significantly closer to that of $g\text{-}C_3N_4$, indicating the presence of interfacial contacts and bonding between the $g\text{-}C_3N_4$ and SnO_2 nanoparticles, thus forming a heterojunction.

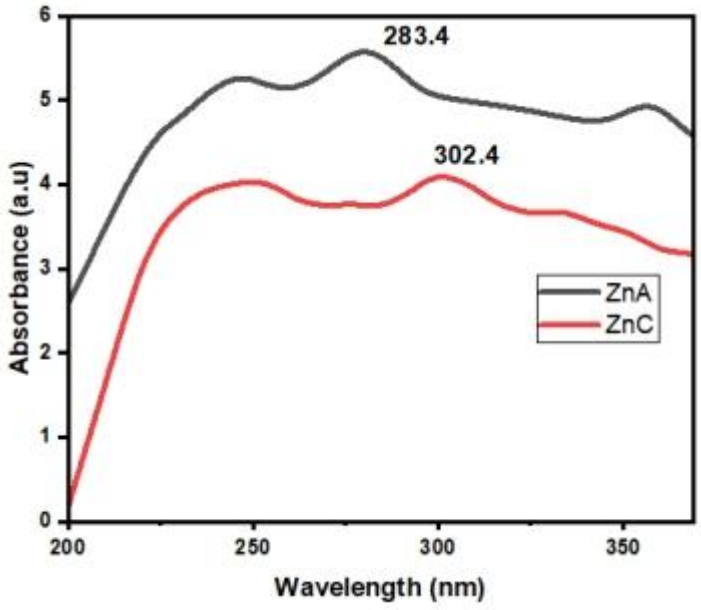

Figure 24. displays the UV-visible spectra of $Ag@SnO_2$ and $Ag@SnO_2/g\text{-}C_3N_4$ nanostructures

Moreover, the energy band-gap (Eg) of ZnA and ZnC nanostructures has been determined using Tauc's relation, as shown in the inset of Figure 24. The band-gap energy of $Ag@SnO_2$ is approximately 2.70 eV, which decreases to 2.44 eV for $Ag@SnO_2/g\text{-}C_3N_4$, as depicted in Figure 25.

This reduction in the band-gap is attributed to the strong interfacial contacts at the heterojunction formed by ZnC and ZnA. Additionally, this parameter may be appealing for reducing the recombination rate of photogenerated electron-hole pairs, potentially enhancing the gas-sensing capabilities of the $Ag@SnO_2/@g\text{-}C_3N_4$ hybrid.

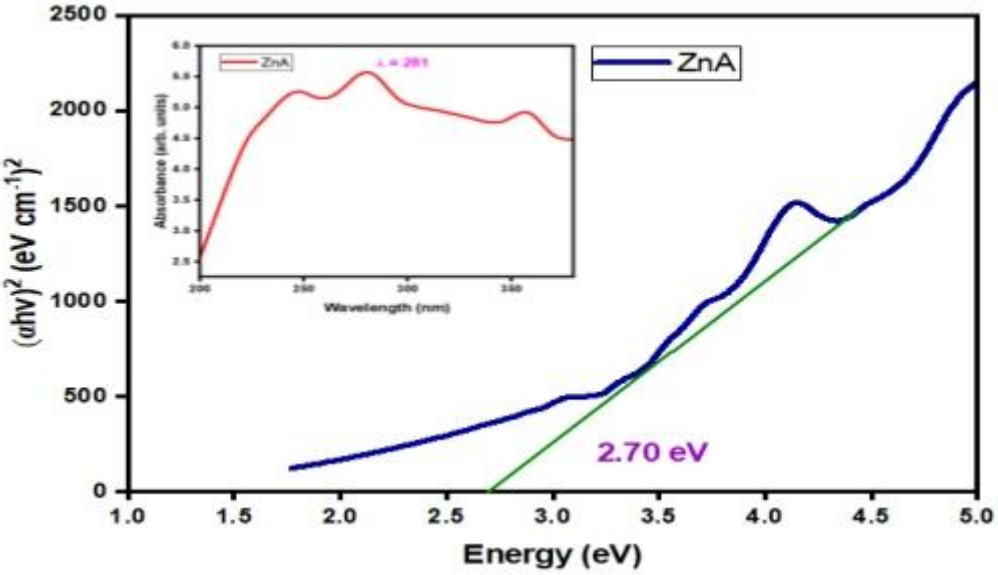

(a)

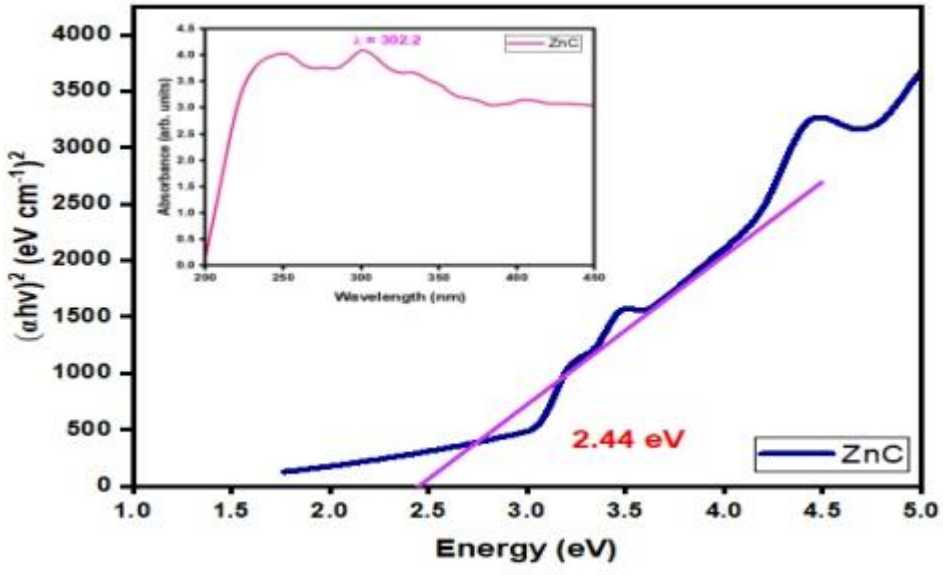

(b)

Figure 25. Tauc's plot of (a) ZnA and (b) ZnC

4.4 FTIR Analysis:

The FTIR spectra (Figure 26) of $Ag@SnO_2$ and $Ag@SnO_2/g\text{-}C_3N_4$ nanostructures were analyzed to elucidate the interactions between the $g\text{-}C_3N_4$ sheets and $Ag@SnO_2$. In the spectra of $Ag@SnO_2/g\text{-}C_3N_4$, a peak at 609 cm^{-1} is observed, indicating the stretching mode of vibrations resulting from the heterocyclic property of the tri-azine unit in $g\text{-}C_3N_4$. Additionally, a band around 480 cm^{-1} is attributed to the anti-symmetric stretching vibration of Sn-O-Sn.

Comparison of the FTIR spectra of $Ag@SnO_2/g\text{-}C_3N_4$ and $Ag@SnO_2$ confirms the production of $g\text{-}C_3N_4$ and $Ag@SnO_2$, respectively. The interactions between SnO_2 nanoparticles and the g-C3N4 sheets result in noticeable shifts in peak positions, confirming the effective production of $Ag@SnO_2/g\text{-}C_3N_4$.

Furthermore, additional peaks, prominent at around 3000-3600 cm^{-1}, are assigned to the N-H and O-H functional groups, indicating that SnO2 is likely to connect to the $g\text{-}C_3N_4$ sheets via hydrogen bonding. The peaks at 1223 cm^{-1}, 1371 cm^{-1}, and 1656 cm^{-1} correspond to intense S=O stretching, OH bending, and C=C stretching, respectively. The faint band observed at 1074 cm^{-1} suggests the formation of Sn-O-C bonds to some extent.

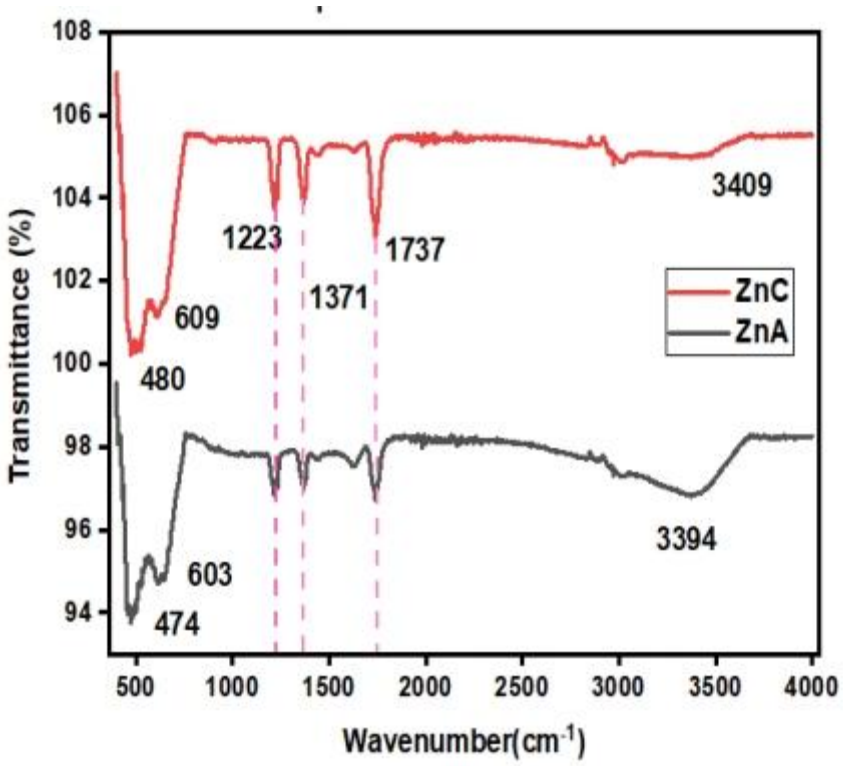

Figure 26. The FTIR spectra of ZnA and ZnC

4.5 Raman Analysis:

Raman spectroscopy was utilized to further confirm the structural properties. A green laser with a spectral width of 535 nm served as the excitation energy source, delivering a few mW of power with sample exposure times of 20 and 120 seconds. To enhance peak clarity, 20X and 50X objective lenses were employed.

The Raman spectra (Figure 27) of ZnC and ZnA exhibit results consistent with FTIR analysis. Both samples display characteristic Raman peaks at 236.5, 566.2, 626.7, and 775.2 cm^{-1} corresponding to the vibration modes of the molecules.

In the ZnC sample, the Raman intensity of the peaks at 566.2 cm^{-1} and around 626.7 cm^{-1} is significantly enhanced, which can be attributed to the surface-enhanced Raman scattering effect of g-C_3N_4. The Raman peaks at 626.7 cm^{-1} and 775.2 cm^{-1} correspond to the breathing modes of the triazine ring.

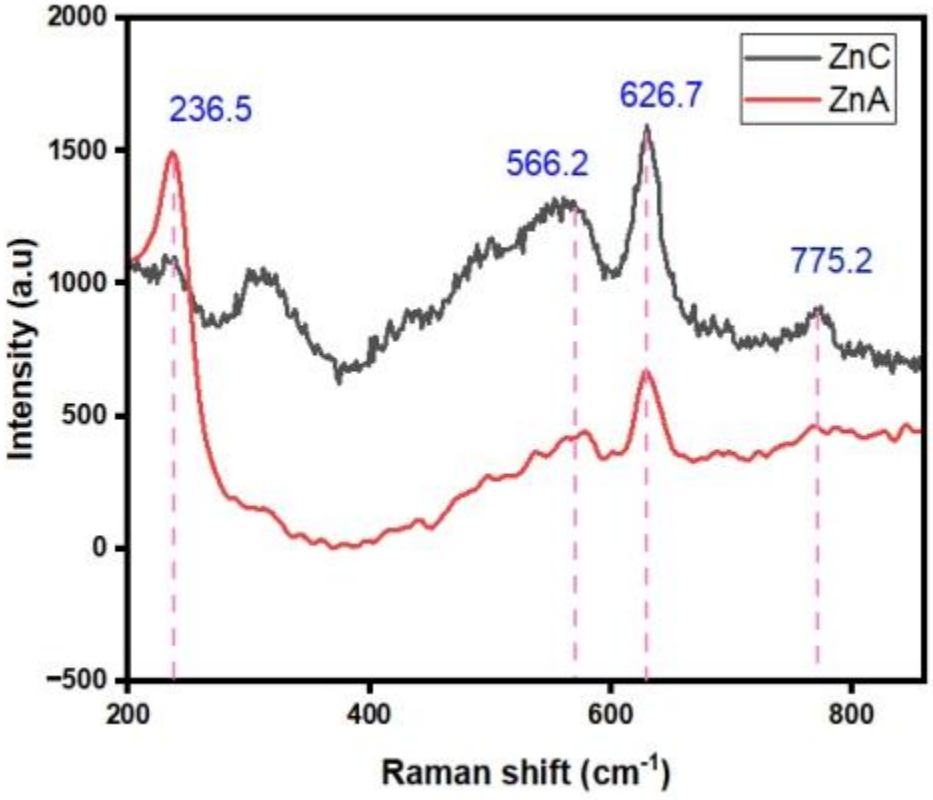

Figure 27. The raman spectra of Ag@SnO_2/g-C_3N_4 and Ag@SnO_2

CHAPTER 5

EXPERIMENTAL SECTION

5.1 Gas-sensing Mechanism

Metal oxide-based compounds have long served as chemiresistive gas sensors, prized for their sensitivity. However, their high operating temperature poses a challenge, particularly in the development of wireless or portable acetone gas sensors. To address this issue, composites combining mixed metal oxides, metal oxide-polymer, and metal oxide have been utilized to lower sensor operating temperatures (16).

A comprehensive study of chemiresistive sensors is carried out to identify state of acetone gas detection. This assessment takes into account the sensor's response and recovery time, and it's sensitivity to acetone gas. This review focuses on analyses of factors influencing the sensing processes of chemiresistive gas sensors toward acetone. Finally, the assessment will end with conclusions and a perspective (17) . Thus, it is hoped that the collection and comparison of information and results from various investigations would lead to a more complete and cohesive understanding of the issue. This endeavor will hopefully lead to further development in the gas-sensing field (18)

In chemiresistive sensors, an active layer sits between two or more electrodes to detect alterations in the electrical resistance of the oxide when exposed to gas. This layer is commonly applied onto a substrate with thickness ranging from 500 nm to 30 μm. Processes such as hydrothermal spin or dip-coating are typically employed to achieve thicknesses below 20 nm (19).

5.1.1 Design:

Figure 28 illustrates the structure of a chemiresistive gas sensor. Typically, the sensor is placed in a quartz chamber for measurements. To ensure good ohmic contact, the sensor is pre-heated and stabilized at high temperatures (300-500 °C) for several hours before measurement (20). During the measurement, the chamber is filled with the target gas, and the current is recorded using a source meter. The resistance signals are monitored using alternating current, reflecting the sensor's dynamic response and recovery

The main charge carrier and the type of gas interacting with the active layer determine whether the oxide's resistance increases or decreases upon exposure to the gas. The sensor's response is governed by the resistivity of the active layer. The definition of response varies by measurement type but is generally defined as the ratio of resistance in air (Ra) to resistance in the presence of the analyte (Rg) for an n-type material with a reducing analyte (21) . For an n-type material with an oxidizing analyte, the response is defined differently. For p-type sensors, the response is defined in the opposite manner (22).

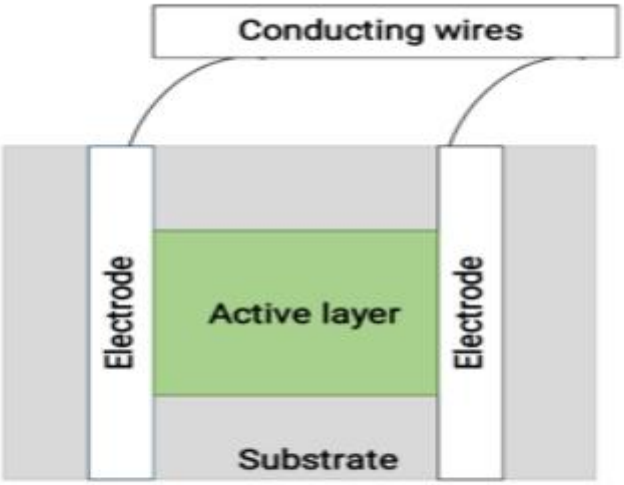

Figure 28. Depicts the chemiresistive gas-sensor structure

5.1.2 General Mechanism:

The responses in this work are reported as Ra/Rg for n-type sensors and Rg/Ra for p-type sensors in order to standardize the evaluation of acetone detection using combined gas sensors. In this case, the resistance of the sensor in air is represented by Ra, and the resistance in the presence of acetone gas is represented by Rg. Despite the fact that many sensors form a p-n heterojunction, they are categorized as either n-type or p-type according to whether the concentration of acetone causes their resistivity to rise or fall (23). For both n-type and p-type gas sensors, this classification guarantees an intelligible comprehension and efficient evaluation of the sensing properties of acetone (24).

The amount of time that the resistance takes to alter and return to 90% of its initial value after coming into contact with the target gas is known as the response time. The amount of time required for a resistance to reach 10% of its highest value after being exposed to air is known as the recovery time. The gas-mixer time must be taken into account in order to assess response and recovery times accurately, as it may be longer than the actual times (25).

The general gas sensing mechanism for metal oxide based acetone gas sensors is as given as:

Initially, when exposed to air, oxygen molecules with high electron affinity adsorb onto the sensor surface. Depending on the operating temperature, different species of oxygen ions will form on the gas sensor surface, as shown by the following equations:

$$O_2\,(g) \longrightarrow O_2\,(ads)$$

$$O_2\,(ads) + e \longrightarrow O_2^-\,(ads)$$

$$O_2^-\,(ads) + e \longrightarrow 2O^-$$

$$2O^- + e \longrightarrow O^{2-}$$

Furthermore, depending on the test-chamber volume and construction, as well as the carrier-gas flow employed in each study, a varied amount of time may be necessary for complete gas displacement (26). As a result, there is no clear way to compare reaction and recovery time. One of the most important properties of any sensor is its response and recovery time, which allows for an accurate assessment of sensing performance. However, most research neglect these properties, particularly in polymer-based gas sensors.

Thus, future investigations should incorporate this study more strategically in order to accomplish comprehensive characterization of acetone gas sensors (27).

Figure 29. **Gas-sensing response of ZnC composite**

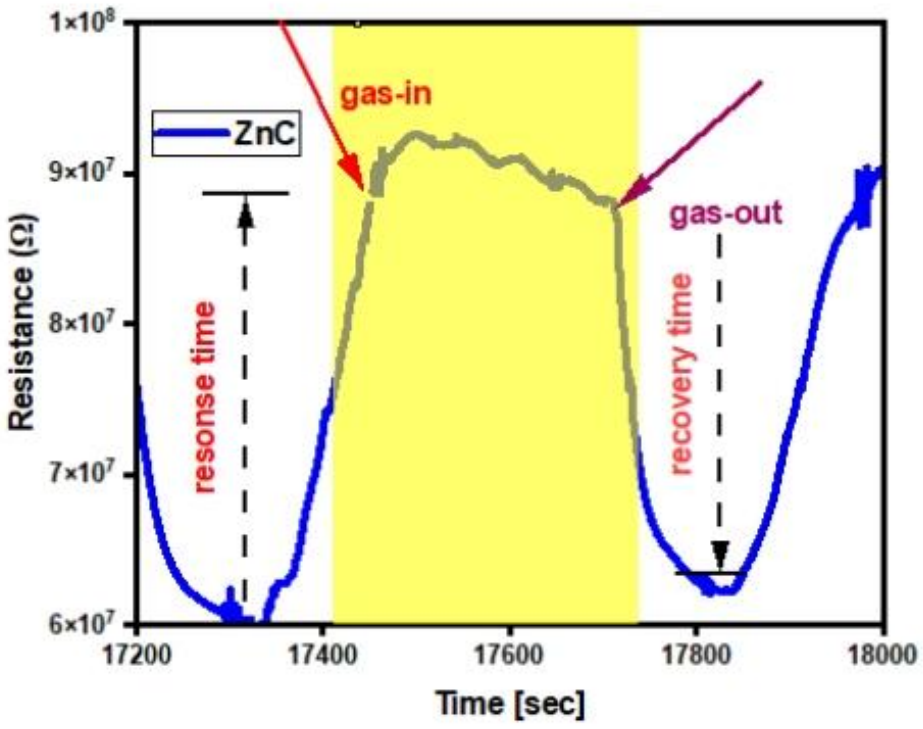

The recovery time of both p-type sensors, Ag/SnO_2 and $Ag@SnO_2/g\text{-}C_3N_4$ had been operated at different temperatures whose response and recover time has been listed below in table 3:

Operating Temperature (℃)	Response Time (sec)		Recovery Time (sec)	
	ZnA	ZnC	ZnA	ZnC
Room Temperature	219.13	29.98	29.18	94.96
50	139.79	9.42	21.66	58.96
100	433.49	119.86	50.26	162.47
125	201.56	94.09	31.09	25.51
150	203.79	54.42	33.72	96.74

Additionally, the p-type metal oxide-carbon composite gas sensor, Ag@SnO2/g-C3N4 nanosheets, demonstrated rapid response and recovery times of 9.42 seconds and 58.96 seconds, respectively, at 100 ppm acetone and an operating temperature of 50℃.

Figure 30 shows Response and recovery time of (a) $Ag@SnO_2$ and (b) $Ag@SnO_2/g\text{-}C_3N_4$ gas sensors for 100ppm acetone at different temperature ranges.

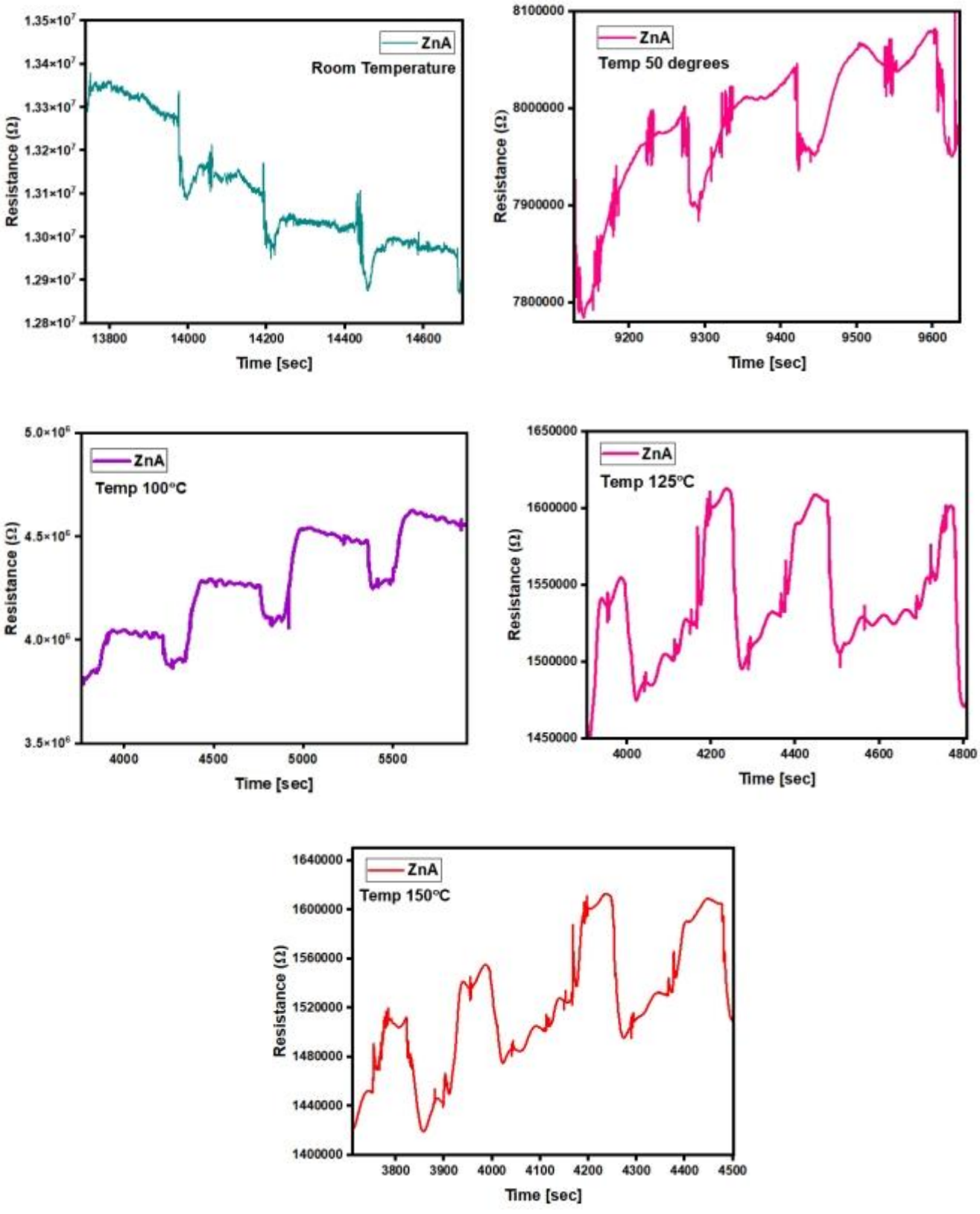

(a) Gas sensing response for ZnA nano-composite

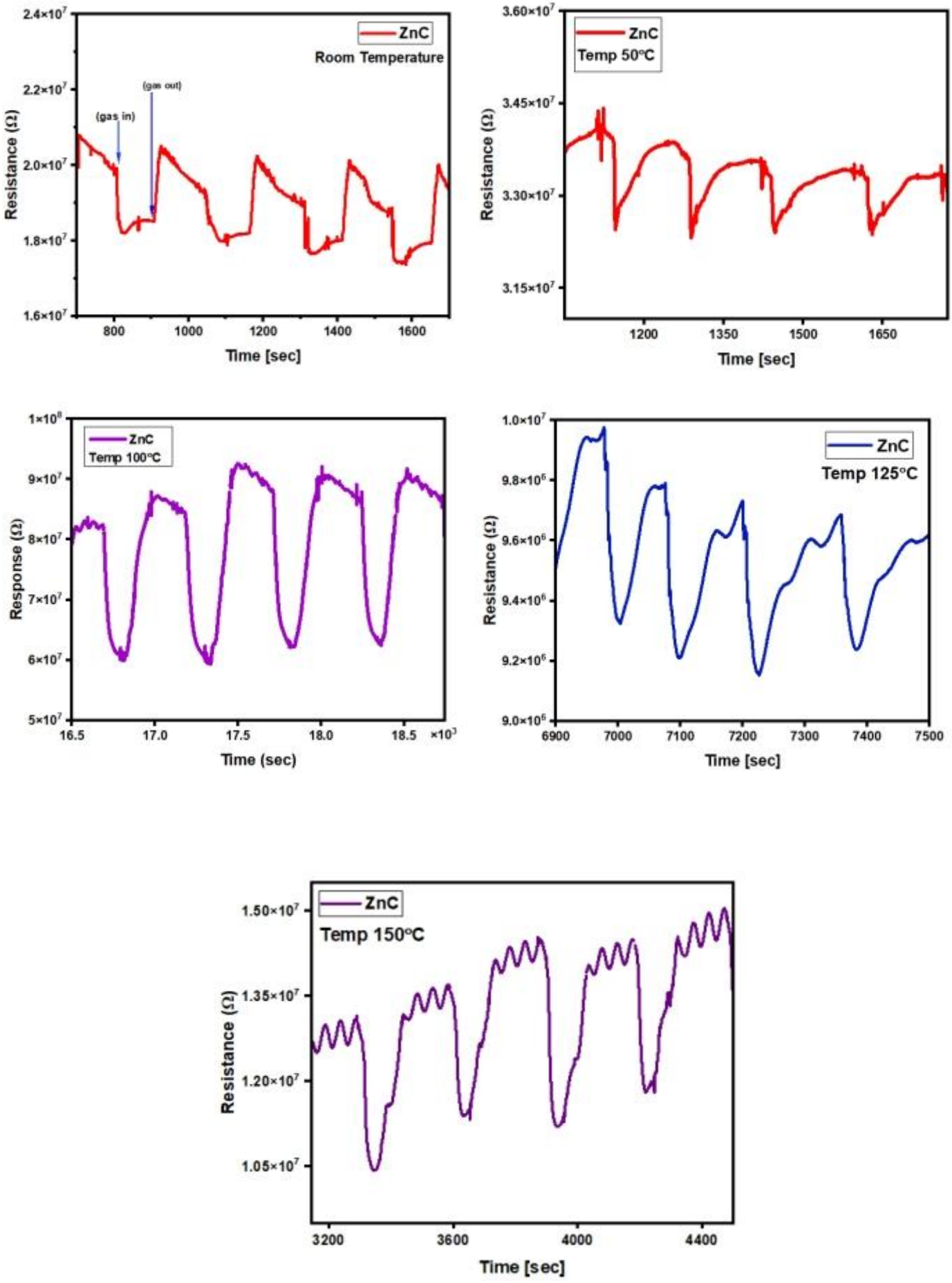

(b) Gas sensing response for ZnC nano-composite

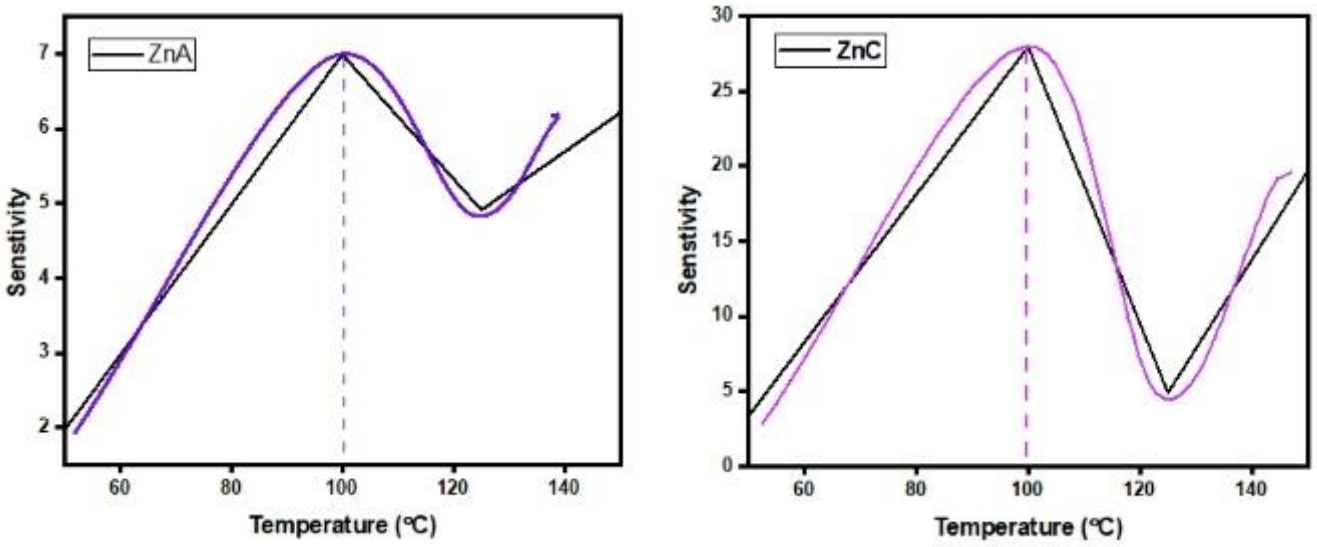

Figure 31. depicts sensitivity curve of (a) ZnA and (b) ZnC

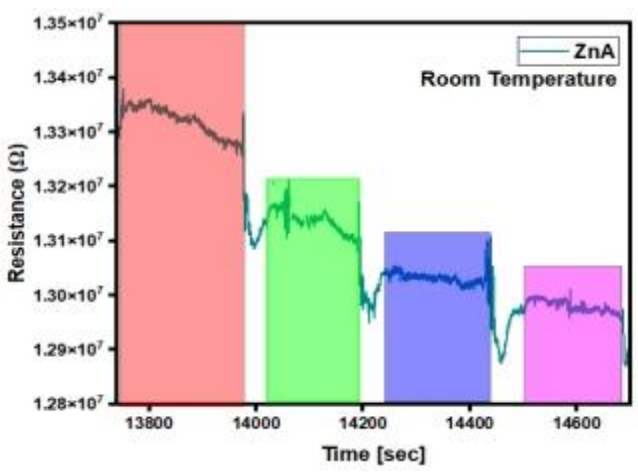

(a)

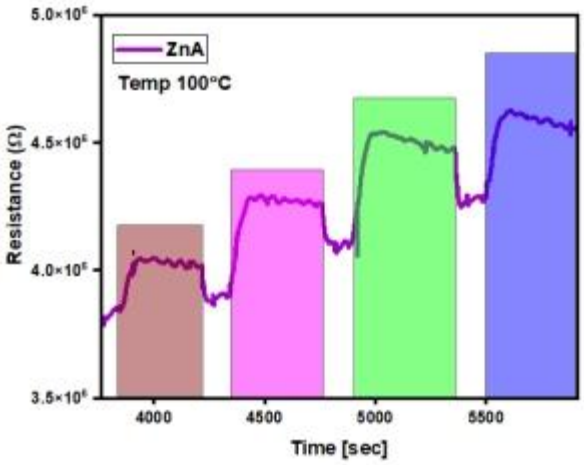

(b)

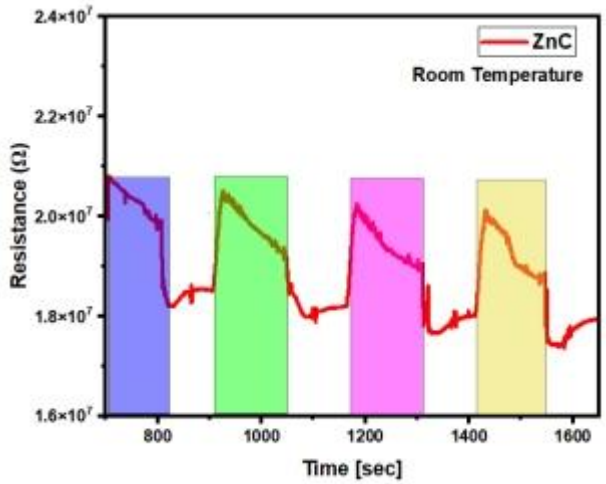

(c)

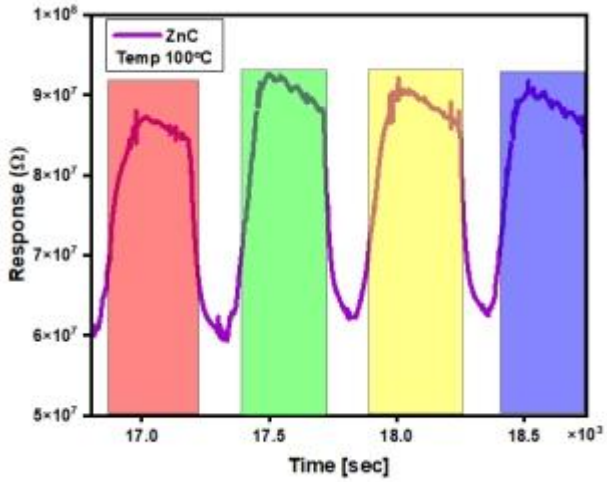

(d)

Figure 32. Gas sensing response of (a-b) ZnA and (c-d) ZnC nanocomposites at room temperature and 100℃ respectively

In Figure 32, there is a possible trend on observing gas sensing resistance vs time graphs that ZnA composite showing decrease in resistance value with respect to time at Room temperature and an increase in resistance value with time at 100℃ . Whereas the values are constant for resistance vs time on operating at room temperature as well as at 100℃ while using ZnC.

5.1.3 Factors influencing acetone gas sensing systems:

The alteration in resistance directly impacts how sensing mechanisms operate. When acetone gas is adsorbed, it triggers a transfer of charge between chemisorbed oxygen and the material surfaces. The interaction between surface oxygen ions and acetone gas forms the basis for detecting acetone (28). The fluctuations in resistance are largely determined by the specific electrical properties of the material's bulk and the reactivity of its solid surface. This indicates that the choice of materials significantly affects the characteristics of chemiresistive sensors (29).

Usually, oxygen molecules present in the surrounding atmosphere undergo chemisorption on the surface of p-type gas sensors. This process leads to the extraction of electrons from the conduction band of the material (30). Consequently, oxygen molecules convert into single or double oxygen ions, which then get ionosorbed on the surface. Consequently, the electron concentration on the surface decreases, resulting in an increase in resistance. However, when a reducing gas like acetone interacts with the ionosorbed oxygen, the extracted electrons are reintroduced into the conduction band, elevating the electron concentration and thereby reducing the resistance (31).

As acetone, a reducing gas, undergoes reaction, electrons are likewise liberated, leading to a reduction in the accumulation layer, consequently causing an elevation in sensor resistance.

Figure 33. show typical mechanisms of p-type gas sensor when exposed to air and acetone gas respectively.

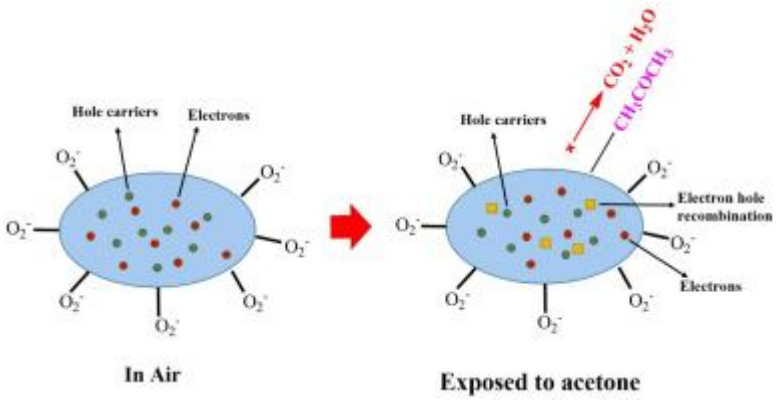

Due to its lack of reactivity at room temperature, the sensor exhibited a low response to acetone. Additionally, the conductivity was ascribed to the interaction between protons and electrons involving ionic species and organic molecules. The magnitude of the sensor's response was linked to the volatile solvent's capacity to donate electrons and accept protons. The organic molecule formed charge-transfer complexes with the substrate, thereby lowering the activation energy required for oxygen chemisorption. Subsequently, the oxygen ion in its reduced state further oxidized the adsorbed organic molecule, consequently releasing electrons into the depletion layer.

Acetone's high molecular weight prevented diffusion into the matrix at ambient temperature, explaining its limited sensor response. In the case of $Ag@SnO_2/g\text{-}C_3N_4$, chemisorption of acetone purportedly led to the formation of partial hydrogen bonds, causing an expansion in interlayer distance. This interruption of the conductive channel resulted in a rise in resistance. Future investigations ought to focus on enhancing acetone reactivity at room temperature, thereby potentially augmenting the sensing response of the metal-oxide nano-composite to acetone (32).

CHAPTER 6

CONCLUSION

Current technological progress has paved the way for the development of high-performance gas sensors based on g-C_3N_4. This research compared stannic oxide semiconductors with the incorporation of g-C_3N_4 into the metal oxide, examining their gas-sensing capabilities for detecting volatile organic compounds, notably acetone. Ag@SnO_2/g-C_3N_4 and Ag@SnO_2 were effectively synthesized using a one-step hydrothermal process, resulting in improved efficiency for target gas detection via a gas-sensing technique. The produced composites were thoroughly examined using XRD, FTIR, UV-Visible, EDX, SEM, and Raman spectra. SEM scans revealed a sheet-like structure of SnO_2/g-C_3N_4, with Ag implanted on top of the sheets. This was validated by EDX analysis, as the Ag content was lower than the SnO_2. Further, the observed response for Ag@SnO_2/g-C_3N_4 and Ag@SnO_2 towards acetone is for 100ppm of acetone, the metal-oxide-based sensor demonstrated rapid response and recovery time. The gas sensing results shows high selectivity towards acetone at 100°C which can be seen from selectivity curve for both ZnA and ZnC composites. The ZnC composite displayed the least response and recovery times of 9.42 s and 58.96 s, respectively, at 50°C, whereas the highest response and recovery times of 119.86 s and 162.4 s, respectively, were observed using ZnC. The outstanding gas sensing performance of the Ag@SnO_2/g-C_3N_4 nanocomposite, featuring an energy band gap of 2.44 eV, can be attributed to several factors: efficient separation of photo-generated electron-hole pairs, the presence of a porous structure in ZnC, a wide surface area, and the formation of SnO_2/g-C_3N_4 p-p junctions. g-C_3N_4, with its large specific surface area, offers numerous active sites for gas molecules, along with high porosity, robust catalytic activity, and effective interaction with stannic oxide. Moreover, the results suggest that the Ag decoration on SnO_2/g-C_3N_4 sheets enhances the specific surface area of the nanocomposites, thereby contributing to the improved sensing response. This heightened response is facilitated by the presence of a porous structure, ample surface area, and the development of SnO_2/g-C_3N_4. A comprehensive analysis of the Ag@SnO_2/g-C_3N_4 nanocomposites underscores their potential as gas sensor materials for detecting acetone vapors at an operating temperature of 100°C.

References :

1 .A, J. o. (2020). Engineering of SnO ₂ –Graphene Oxide Nanoheterojunctions for Selective Room-Temperature Chemical Sensing and Optoelectronic Devices. *ACS Applied Materials & Interfaces*.

2. Ahmad, K. (2023). Synthesis of tin oxide (SnO2) for the fabrication of voltammetric hydrazine sensor. *Materials Chemistry and Physics*.

3. Akhir, M. A. (2019). ScienceDirect Synthesis of SnO 2 Nanoparticles via Hydrothermal Method and Their Gas Sensing Applications for Ethylene Detection. 810.

4. Akhtar, K. (2018). Scanning electron microscopy: Principle and applications in nanomaterials characterization. *Handbook of Materials Characterization*.

5. Baharuddin, A. A. (2019). Advances in chemiresistive sensors for acetone gas detection. *Materials Science in Semiconductor Processing*.

6. Fang, H. B. (2016). Facile Large-Scale Synthesis of Urea-Derived Porous Graphitic Carbon Nitride with Extraordinary Visible-Light Spectrum Photodegradation. *Industrial and Engineering Chemistry Research*.

7. Fang, H. B. (2016). Facile Large-Scale Synthesis of Urea-Derived Porous Graphitic Carbon Nitride with Extraordinary Visible-Light Spectrum Photodegradation. *Industrial and Engineering Chemistry Research*.

8. Fu, Q. (2023). Advances in the development of MOS-based sensors for detection of ethanol: A review. *Materials Research Bulletin*.

9. Guo, L. (2023). One-step hydrothermal synthesis of uniform Ag-doped SnO2 nanoparticles for highly sensitive ethanol sensing. *Physica E: Low-Dimensional Systems and Nanostructures*.

10. Guo, L. (2023). One-step hydrothermal synthesis of uniform Ag-doped SnO2 nanoparticles for highly sensitive ethanol sensing. *Physica E: Low-Dimensional Systems and Nanostructures*.

11. He, Y. (2021). Effect of Ag doping on SnO2 sensing for detecting H2S: A first-principles study. *Vacuum*.

12. Kushwaha, A. (2024). Chemiresistive gas sensors beyond metal oxides: Using ultrathin two-dimensional nanomaterials. *FlatChem*.

13. Lawaniya, S. D. (2023). Functional nanomaterials in flexible gas sensors: recent progress and future prospects. *Materials Today Chemistry*.

14. Lete, C. (2020). Nitrite electrochemical sensing platform based on tin oxide films. *Sensors and Actuators B: Chemical*.

15. Liu, X. (2019). SnO2 nanocrystallines decorated g-C3N4 composites with enhanced visible-light photocatalytic activity. *Integrated Ferroelectrics*.

16. Mirzaei, A. (2016). Detection of hazardous volatile organic compounds (VOCs) by metal oxide nanostructures-based gas sensors: A review. *Ceramics International*.

17. Mohammad, A. (2019). Biofilm-Assisted Fabrication of Ag@SnO2- g-C3N4 Nanostructures for Visible Light-Induced Photocatalysis and Photoelectrochemical Performance. *Journal of Physical Chemistry C*.

18. Mohammad, A. (2019). Biofilm-Assisted Fabrication of Ag@SnO2- g-C3N4 Nanostructures for Visible Light-Induced Photocatalysis and Photoelectrochemical Performance. *Journal of Physical Chemistry C*.

19. Mohammad, A. (2019). Synergistically effective and highly visible light responsive SnO2-g-C3N4 nanostructures for improved photocatalytic and photoelectrochemical performance. *Applied Surface Science*.

20. Pazouki, S. (2021). Effects of Hydrothermal temperature on the physical properties and anomalous band gap behavior of ultrafine SnO2 nanoparticles. *Optik*.

21. Pradeev raj, K. (2018). Influence of Mg Doping on ZnO Nanoparticles for Enhanced Photocatalytic Evaluation and Antibacterial Analysis. *Nanoscale Research Letters*.

22. Rafique, M. S. (2020). Synthesis methods of nanostructures. *Nanotechnology and Photocatalysis for Environmental Applications*.

23. Rahman, M. A. (n.d.). A Review on Semiconductors Including Applications and Temperature Effects in Semiconductors.

24. Research, I. a. (2019). Synergistically effective and highly visible light responsive SnO2-g-C3N4 nanostructures for improved photocatalytic and photoelectrochemical performance. *Applied Surface Science*.

25. Rumchev, K. (2007). Volatile organic compounds: Do they present a risk to our health? *Reviews on Environmental Health*.

26. Saravanakumar, K. (2017). Fabrication of sphere like plasmonic Ag/SnO2 photocatalyst for the degradation of phenol. *Optik*.

27. Sharma, R. (2012). X-ray diffraction: a powerful method of characterizing nanomaterials. *Applied Surface Science*.

28. Sinha, T. (2017). Green and Environmentally Sustainable Fabrication of Ag-SnO2 Nanocomposite and Its Multifunctional Efficacy As Photocatalyst and Antibacterial and Antioxidant Agent. *ACS Sustainable Chemistry and Engineering*.

29. Srinivasan, P. (2021). Insights into g-C ₃ N ₄ as a chemi-resistive gas sensor for VOCs and humidity – a review of the state of the art and recent advancements. *Journal of Materials Chemistry A*.

30. Vander Wal, R. L. (2009). Metal-oxide nanostructure and gas-sensing performance. *Sensors and Actuators, B: Chemical*.

31. Wang, Z. (2021). One-dimensional nanomaterials in resistive gas sensor: From material design to application. *Chemosensors*.

32. Zhang, J. (2016). A brief review of co-doping. *Frontiers of Physics*.

iSNIOE² 2024

INTERNATIONAL CONFERENCE ON SUSTAINABLE NANOMATERIALS INTEGRATION & ORGANIZATION FOR ENERGY AND ENVIRONMENT

SHIV NADAR UNIVERSITY DELHI NCR

We are pleased to present the

CERTIFICATE OF PARTICIPATION

to

Anshika Goyal

for giving the **poster presentation** on their work titled "*g-C3N4 modified Ag@SnO2 heterostructures – a potential resistive gas sensor towards VOCs*" in the International conference on Sustainable Nanomaterials Integration & Organization for Energy and Environment organised by Department of Physics, School of Natural Science (SNS), Shiv Nadar Institution of Eminence (SNIoE) Deemed to be University, Delhi NCR held during 20-23 March 2024.

Prof. Aloke Kanjilal
Co-Chairperson

Dr. Binson Babu
Convenor

Jointly organized in collaboration with

KTH ROYAL INSTITUTE OF TECHNOLOGY · UNSW SYDNEY

iSNIOE² 2024

INTERNATIONAL CONFERENCE ON SUSTAINABLE NANOMATERIALS INTEGRATION & ORGANIZATION FOR ENERGY AND ENVIRONMENT

SHIV NADAR UNIVERSITY DELHI NCR

We are pleased to present the

CERTIFICATE OF PARTICIPATION

to

Yoshita Katiyar

for giving the **poster presentation** on their work titled "*g-C3N4 modified Ag@SnO2 heterostructures – a potential resistive gas sensor towards VOCs*" in the International conference on Sustainable Nanomaterials Integration & Organization for Energy and Environment organised by Department of Physics, School of Natural Science (SNS), Shiv Nadar Institution of Eminence (SNIoE) Deemed to be University, Delhi NCR held during 20-23 March 2024.

Prof. Aloke Kanjilal
Co-Chairperson

Dr. Binson Babu
Convenor

Jointly organized in collaboration with

KTH ROYAL INSTITUTE OF TECHNOLOGY · UNSW SYDNEY

PAPER NAME

plag report paper.docx

WORD COUNT	CHARACTER COUNT
7578 Words	43686 Characters
PAGE COUNT	FILE SIZE
44 Pages	2.8MB
SUBMISSION DATE	REPORT DATE
Jun 5, 2024 1:06 AM GMT+5:30	Jun 5, 2024 1:07 AM GMT+5:30

15% Overall Similarity

The combined total of all matches, including overlapping sources, for each database.

- 6% Internet database
- 8% Publications database
- Crossref database
- Crossref Posted Content database
- 9% Submitted Works database

Excluded from Similarity Report

- Manually excluded sources

15% Overall Similarity

Top sources found in the following databases:

- 6% Internet database
- Crossref database
- 9% Submitted Works database
- 8% Publications database
- Crossref Posted Content database

TOP SOURCES

The sources with the highest number of matches within the submission. Overlapping sources will not be displayed.

1	mdpi.com Internet	<1%
2	encyclopedia.pub Internet	<1%
3	"Extraction 2018", Springer Science and Business Media LLC, 2018 Crossref	<1%
4	Akbar Mohammad, Md Rezaul Karim, Mohammad Ehtisham Khan, Moh... Crossref	<1%
5	Ze Wang, Lei Zhu, Shiyi Sun, Jianan Wang, Wei Yan. "One-Dimensional ... Crossref	<1%
6	Higher Education Commission Pakistan on 2022-08-11 Submitted works	<1%
7	Indian Institute of Technology Jodhpur on 2020-05-25 Submitted works	<1%
8	University of Derby on 2023-11-24 Submitted works	<1%

9	iris.polito.it Internet	<1%
10	Ohio State University on 2013-11-11 Submitted works	<1%
11	coek.info Internet	<1%
12	link.springer.com Internet	<1%
13	Dipyaman Mohanta, Md. Ahmaruzzaman. "Novel Ag-SnO2-βC3N4 tern... Crossref	<1%
14	K.W. Koch. "Group velocity dispersion measurements of microstructur... Crossref	<1%
15	Rhodes University on 2022-09-06 Submitted works	<1%
16	openscholarship.wustl.edu Internet	<1%
17	giiresearch.com Internet	<1%
18	gossmanforensics.com Internet	<1%
19	SASTRA University on 2015-05-07 Submitted works	<1%
20	University of KwaZulu-Natal on 2024-03-05 Submitted works	<1%

33	Kyungju Nam, Hyeong-Gwan Kim, Hyelim Choi, Hyeji Park, Jin Soo Kan... Crossref	<1%
34	University of Southampton on 2023-05-11 Submitted works	<1%
35	ethesis.nitrkl.ac.in Internet	<1%
36	repositori.usu.ac.id:8080 Internet	<1%
37	Institute of Cancer Research on 2011-01-24 Submitted works	<1%
38	upcommons.upc.edu Internet	<1%
39	intechopen.com Internet	<1%
40	Rashmi J. Nayak, Jyotiprakash G. Nayak. "TSDC and EDX studies of pu... Crossref	<1%
41	Yao-Tien Tseng, Jing-Chie Lin, Yong-Jie Ciou, Yean-Ren Hwang. "Fabri... Crossref	<1%
42	cyberleninka.org Internet	<1%
43	coursehero.com Internet	<1%
44	B. Amudhavalli, R. Mariappan, M. Prasath, R. N. Jayaprakash. "Fabricat... Crossref	<1%